Journal of Materials Processing Tech. 344 (2025) 119000

Contents lists available at ScienceDirect

Journal of Materials Processing Tech.

journal homepage: www.elsevier.com/locate/jmatprotec

Research article

A novel flexible-structured saw blade for bone cutting: reducing ploughing and promoting chip evacuation

Han Wang, Urara Satake *, Toshiyuki Enomoto

Division of Mechanical Engineering, Graduate School of Engineering, The University of Osaka, 2-1, Yamada-oka, Suita, Osaka 565-0871, Japan

ARTICLE INFO

Keywords:
Bone cutting
Flexible-structured blade
Passive vibration-assisted cutting
Ploughing force reduction
Chip evacuation

ABSTRACT

Oscillating bone sawing is widely employed in orthopedic surgery due to its ability to achieve precise bone resection with minimal damage to surrounding soft tissues. However, conventional saw blades with large negative rake angles often induce excessive ploughing forces, elevated temperatures, poor chip evacuation, accelerated tooth tip wear, and crack formation in bone tissue. While trajectory and vibration-assisted strategies have been explored, their reliance on complex mechanical systems limits clinical adoption. In this study, a novel saw blade with an embedded flexible structure is proposed, which passively adjusts the depth of cut through elastic deformation of the flexible structure. This design offers two key advantages: (1) when cutting with a negative rake face, the flexible tooth adaptively reduces the actual depth of cut, thereby reducing ploughing forces; and (2) when cutting with a positive rake face, periodic elastic deformation induces passive low-frequency vibrations, promoting shear crack formation and transforming continuous, spiral-like chips into fine, needle-like fragments, thereby improving chip evacuation. Multi-tooth sawing experiments confirmed that the proposed blade reduced sawing forces by 56.4 % in the feed direction and 36.7 % in the oscillation direction, suppressed peak cutting temperature to 43.3 °C (below the 47 °C threshold for cell damage), and significantly decreased tooth tip wear and groove wall cracking. These results demonstrate the effectiveness of the proposed structure as a compact, mechanically simple solution that complements motion-based strategies, enhancing cutting performance and adaptability in bone cutting applications.

1. Introduction

Oscillating and reciprocating bone sawing techniques are widely employed in orthopedic procedures such as fracture repair, joint replacement, and orthognathic surgery. These methods enable precise bone cutting in anatomically constrained regions and offer superior preservation of soft tissues due to their limited rotation compared to rotary cutting tools [1]. Recent advances in reciprocating motion for bone drilling systems have reported improved prevention of soft tissue entanglement around the drill [2], reinforcing the value of oscillatory modes in surgical applications. However, oscillating bone sawing presents several inherent challenges that hinder cutting efficiency: (1) elevated cutting forces, which accelerate blade wear [3,4] and increase bone damage [3]; (2) inefficient chip evacuation, which leads to tool clogging and reduced cutting performance [5]; and (3) excessive frictional heating, which can elevate local temperatures and cause thermal damage to surrounding tissues [6,7]. These issues compromise surgical precision, cutting efficiency, and long-term implant stability [8,9], highlighting the need for improved cutting force control, chip evacuation, and thermal management strategies in oscillating bone sawing.

To develop effective solutions, a fundamental understanding of how cortical bone responds to cutting at different scales is essential. The hierarchical microstructure of cortical bone governs its deformation and fracture behaviors during mechanical loading. At the macro-scale (10–500 μm), this collagen-hydroxyapatite composite undergoes brittle fracture [10], which leads to unstable crack propagation during orthogonal cutting at large depths of cut (20–200 μm) [11]. In contrast, at sub-micron scales (1–10 μm), the cortical bone exhibits ductile characteristics [12,13], including elastic recovery and viscoelastic deformation when cutting at small depths of cut (5–20 μm) with negative rake angles [14]. Based on these scale-dependent behaviors, three primary strategies have been proposed in rotary bone cutting to reduce cutting forces and thermal accumulation: (1) controlling crack propagation, as demonstrated by Sugita and Mitsuishi [15,16], which minimizes energy

* Corresponding author.
E-mail addresses: wanghan@cape.mech.eng.osaka-u.ac.jp (H. Wang), satake@mech.eng.osaka-u.ac.jp (U. Satake), enomoto@mech.eng.osaka-u.ac.jp (T. Enomoto).

https://doi.org/10.1016/j.jmatprotec.2025.119000
Received 18 May 2025; Received in revised form 29 July 2025; Accepted 29 July 2025
Available online 5 August 2025

dissipation but requires precise crack initiation control, posing a challenge under dynamic surgical conditions; (2) optimizing depth-of-cut, as explored by Liao and Axinte [11], which promotes fracture-dominant material removal but is highly dependent on bone geometry and cutting depth control; and (3) introducing vibration-assisted cutting, as proposed by Alam et al. [17], which promotes crack propagation but may rely heavily on proper frequency tuning and tool stiffness. To implement these strategies, various tool designs have been developed in rotary cutting, such as multi-scale cutting edges [18], spiral micro-edge profiles [19], and vibration-assisted methods [20,21]. However, their direct application to oscillating sawing stays limited due to fundamentally different tool kinematics and force interactions.

Due to the reciprocating motion of oscillating saws, saw teeth typically operate with a negative rake angle [14], which strongly influences cutting force [22], temperature rise [23], chip evacuation [5], and tool wear [3]. These adverse outcomes are primarily attributed to ploughing effects induced by the large negative rake angle [24,25], which generate excessive thrust forces and hinder effective chip formation [14]. To mitigate localized stress and reduce saw tooth wear, conventional blades are often designed with a greater number of teeth and smaller tooth pitches, which helps distribute loads more evenly across individual teeth. However, this configuration reduces the interdental gullet volume, thereby limiting chip storage and hindering evacuation. The resulting chip accumulation further increases cutting forces and raises temperatures [5,26]. These coupled effects reveal an inherent trade-off in conventional blade design—efforts to reduce localized loading on each tooth through increased tooth count may inadvertently compromise chip evacuation and thermal regulation.

To overcome these challenges, various motion-based strategies have been proposed. For example, James et al. [27] introduced a figure-eight orbital motion to an oscillating bone saw, which improved cutting efficiency. However, increasing cutting depth to improve efficiency may inadvertently generate excessive impact force [22] and undesired crack propagation into the bone [28]. Shu et al. [28] investigated elliptical vibration-assisted oscillating bone sawing and reported reduced sawing forces compared to conventional oscillating motion. However, higher vibration frequencies led to increased frictional heating [29]. Wang et al. [3] proposed an oscillating trajectory with elliptical-like paths near the oscillation extremes, which effectively reduced ploughing forces by decreasing the depth of cut when using a negative rake angle. Despite their benefits, these motion-based strategies often increase mechanical complexity. The additional hardware requirements may enlarge device size and weight, making them less suitable for minimally invasive or robotic surgery. In contrast, improving the design of the saw blade itself, where the part is in direct contact with the bone, offers a more compact and mechanically simpler solution. However, conventional blades with rigid structures lack the compliance needed to adapt to varying cutting resistance or to facilitate chip removal dynamically. These limitations underscore the need for a structurally adaptive solution that mitigates cutting forces and improves chip evacuation without increasing device complexity.

To bridge this gap, this study proposes a novel flexible-structured saw blade designed to improve bone cutting performance. This innovative blade structure enables passive adjustment of cutting depth through elastic deformation during operation. This structural response leads to two key improvements: (1) when cutting with the negative rake face, the flexible tooth adaptively reduces the actual depth of cut, significantly lowering ploughing forces; and (2) when cutting with the positive rake face, elastic energy accumulation and release induce passive low-frequency vibrations, which facilitate shear-crack plane formation and promote the generation of needle-like chips, thereby improving chip evacuation. Experimental validation under multi-tooth sawing conditions confirmed that the proposed blade structure significantly improved sawing performance. It reduced overall sawing force and temperature rise, limited tooth wear, and suppressed crack propagation along groove walls. These results suggest that a structure-based design strategy, rather than one reliant on added motion complexity, can offer a practical and effective solution for enhancing cutting performance and surgical adaptability in bone cutting applications.

2. Challenges in conventional bone saw blade

While previous studies have linked performance limitations to negative rake angles and inefficient chip evacuation, a more detailed understanding can be obtained by analyzing the geometric features of conventional oscillating saw blades, which influence both cutting mechanics and chip evacuation behavior. As shown in Fig. 1a, sawing process involves a blade oscillating around a pivot point, causing each tooth tip to follow a circular arc. To ensure uniform loading, commercial blades often adopt a curved cutting edge, aligning all teeth with a consistent oscillation radius. Two typical rake configurations are commonly used: blades either incorporate a nominally positive rake face at the tooth tip (Fig. 1b) or employ fully negative rake design (Fig. 1c). Regardless of the nominal rake angle, the reciprocating motion leads to engagement of the flank face at a large effective negative rake angle, thereby including pronounced ploughing effects.

2.1. Ploughing effect

According to previous studies [22,24], the total cutting force during cortical bone cutting consists of three components: shear force from the shear layer, ploughing force from the rounded cutting edge, and ploughing force from the negative rake face in the ploughing layer. As shown in Fig. 2, when using a large negative rake angle, the resultant cutting force increases linearly with cut depth due to the large ploughing layer. Notably, the specific cutting force—defined as energy consumed per unit volume of material removed in bone cutting [11]—remains relatively constant across varying cutting depths, suggesting that ploughing is the dominant contributor to cutting resistance. The resulting high forces may cause plastic deformation or premature wear of the tooth tip, especially considering the typically small lip angle (approximately 50°) of oscillating saw teeth. On the other hand, when using a positive or zero rake angle, both the resultant and specific cutting forces are significantly lower than those observed with a negative rake angle at relatively large depths (5–20 μm). However, ploughing persists due to the presence of a rounded cutting edge, yielding cutting forces that are comparable to those observed under large negative rake conditions. These results indicate that rake angle modification alone is insufficient to reduce ploughing, underscoring the structural limitations imposed by the cutting edge geometry.

In conventional saw blade design, increasing the number of tooth tips (i.e., reducing the tooth pitch) and raising the oscillation frequency are commonly adopted strategies to reduce the depth of cut per tooth, thereby lowering the local load on each tooth and mitigating tooth tip wear during cutting. However, such reductions in cutting depth often lead to higher overall cutting forces due to the increased specific cutting force in the ploughing-dominated regime. Fig. 3a shows the machined area of a single tooth at different pitch conditions. The maximum depth of cut in the oscillating cycle ($h(t_1)$) depends on the pitch (Fig. 3b) and can be expressed as [22]:

$$h(t_1) = 2V_{feed}(t_1 - t_0)\cos(\omega + \theta_{t_1}) \tag{1}$$

where V_{feed} is the feed speed; ω is the angular separation between two adjacent teeth, approximated as $\omega \approx \arcsin(L_{Pitch}/R)$, with pitch distance ($L_{Pitch}$) and oscillating radius (R); t_0 is a quarter cycle time ($t_0 = 1/(4f)$, f is oscillation frequency of the oscillating saw); θ_t is the variation of oscillation angle with time ($\theta_t = A\sin(2\pi f t_1)$, A is the oscillation angle); t_1 is the time at which the tooth begins to overlap with its adjacent tooth, determined by solving the Y-axis motion condition [22]:

$$Y_i(t_1) = \sin(\theta_{t_1} + \omega)R = Y_{i-1}(t_0) = \sin(\theta_{t_0})R \tag{2}$$

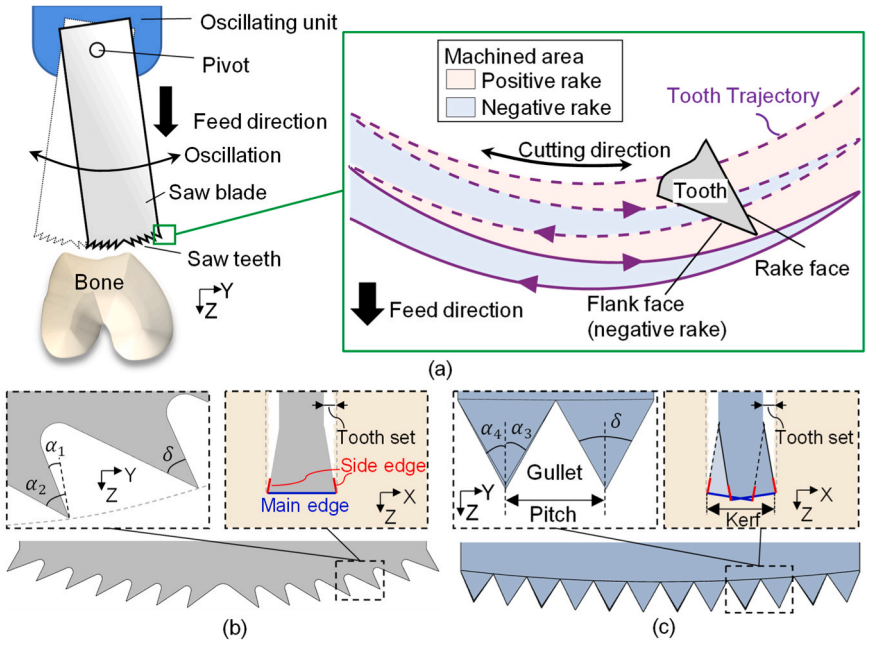

Fig. 1. (a) Schematic of the oscillating sawing process: the blade reciprocates laterally at high frequency while feeding into the workpiece. (b, c) Blade geometries with different rake configurations: (b) positive rake angle and (c) negative rake angle. The rake angle (α) and lip angle (δ) define tooth edge geometry, affecting chip formation and cutting forces. The kerf width exceeds the blade thickness due to the tooth set—an alternating offset that reduces friction and facilitates chip evacuation. The small depth of cut limits side-edge engagement, concentrating loads on the main cutting edge at the tooth tip [23].

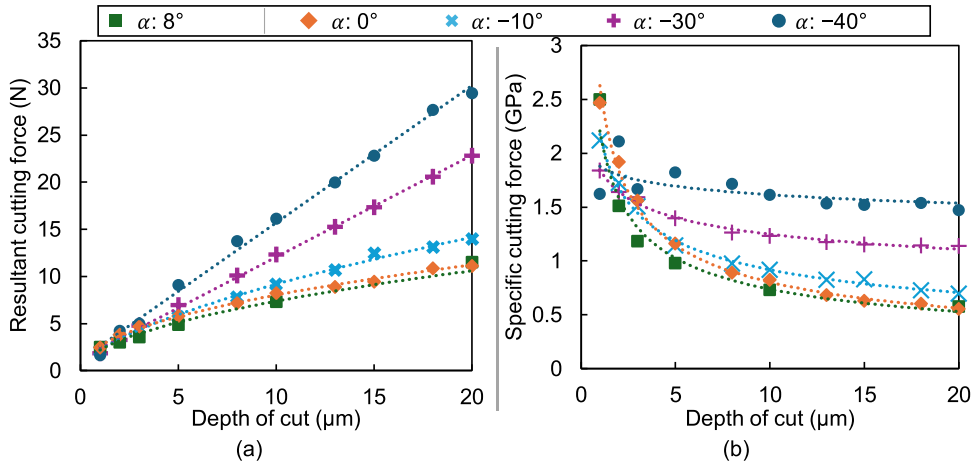

Fig. 2. (a) Resultant cutting force and (b) specific cutting force at different depths of cut with different rake angles from [22,24]. Cutting width: 1 mm. Tested rake angles: $\alpha = 8°$ [24] and $\alpha = 0°, -10°, -30°, -40°$ [22].

Therefore, the correspondence between pitch, maximum depth of cut and number of teeth is shown in Fig. 3c. The corresponding sawing forces, estimated from Figs. 2 and 3c, show that increasing the tooth pitch from 2 mm to 4 mm reduces the sawing force by 30.7–32.8 % (Fig. 3d). The results suggest that increasing the tooth pitch moderately is an effective strategy for reducing total sawing force, as it increases the depth of cut per tooth and thus reduces the relative influence of ploughing. In contrast, increasing the rake angle from −10° to 0°—although geometrically more aggressive—resulted in a 10.6–11.4 % increase in total force. This is primarily due to enhanced ploughing on the flank face during reverse cutting phase, reinforcing the conclusion that rake angle modification alone is insufficient for force reduction when flank-face ploughing dominates.

2.2. Crack formation

Excessive ploughing also induces mechanical damage to bone tissues, particularly through the initiation of cracks. As illustrated in Fig. 4, when the thrust force is concentrated, especially under high ploughing conditions, cracks tend to initiate on the groove bottom and wall surfaces. Bottom cracks primarily propagate along the feed direction due to localized tensile and shear stresses. Their formation follows a mixed-mode fracture mechanism involving both Mode I (tensile opening) and Mode II (in-plane shearing) components [11,14]. However, these cracks are typically shallow and transient, as the groove bottom is continuously removed by the subsequent oscillation cycles.

In contrast, groove wall cracks are more persistent and pose greater clinical risks. The thrust force generated by ploughing can be redirected toward the wall, promoting Mode I fracture perpendicular to the wall surface. Notably, the Mode I fracture toughness of cortical bone is

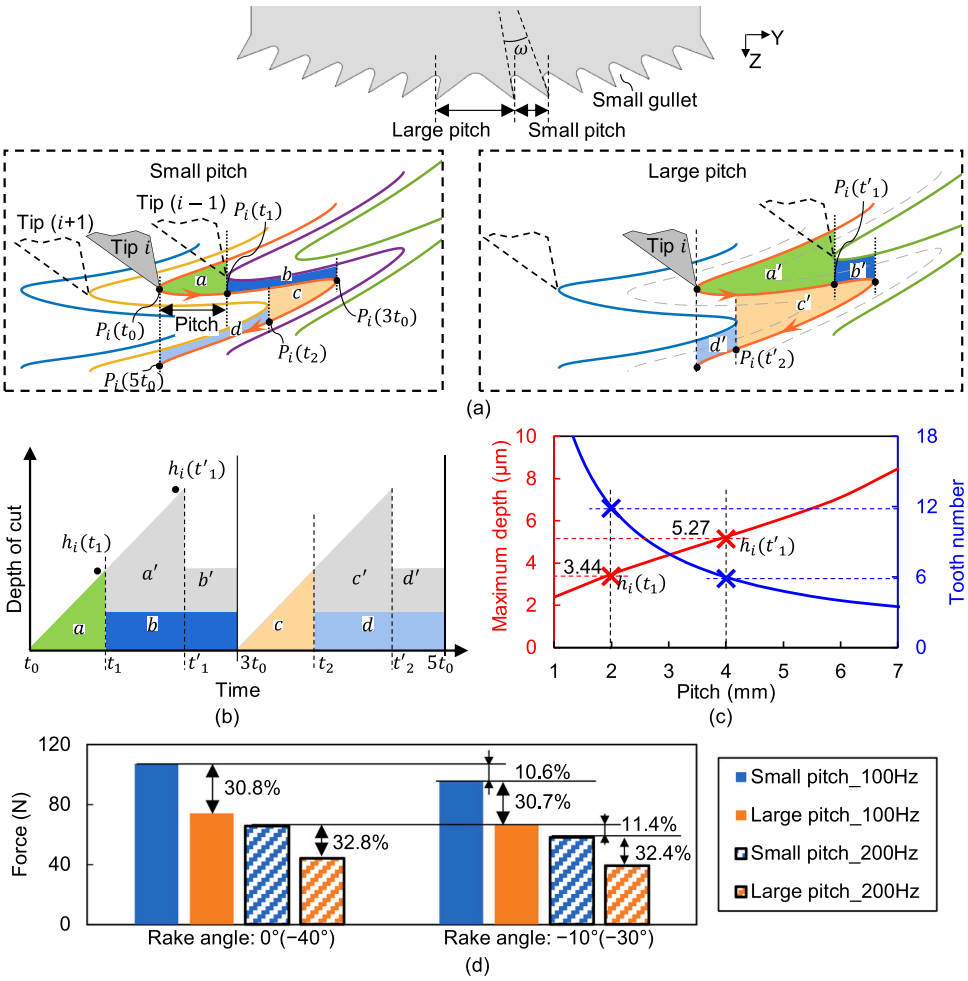

Fig. 3. Relationship between pitch and depth of cut of single saw tooth: (a) Machined area of a single tooth tip when using different pitch conditions; (b) Variation of depth of cut over time within one oscillation cycle; (c) Maximum depth of cut and number of teeth under different pitch settings. (d) Estimated sawing force for different pitch and tooth rake angle settings. General parameters in clinical settings [22,28]: V_{feed}: 2 mm/s; f: 100, 200 Hz; R: 85 mm; A: 2.5°; small pitch (commonly used): 2 mm ($h(t_1)$: 3.44 μm (200 Hz), 6.88 μm (100 Hz); number of teeth: 12). Large pitch: 4 mm ($h(t'_1)$: 5.27 μm (200 Hz), 10.54 μm (100 Hz), number of teeth: 6). Cutting force per tooth was obtained from Fig. 2. Total sawing force was estimated assuming that half the teeth cut on the rake face (rake angle: −10°, 0°), while the other half cut on the flank face (rake angle: −30°, −40°).

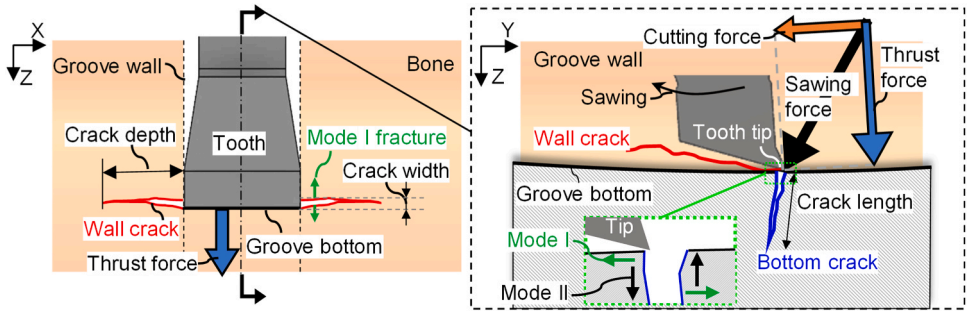

Fig. 4. Schematic illustration of crack formation under excessive sawing force. High thrust forces induced by ploughing cause crack initiation at both the groove bottom and wall. Bottom cracks propagate laterally or downward under mixed-mode loading [14], while wall cracks extend perpendicularly under Mode I fracture driven by tensile stress.

approximately one-fourth of that under Mode II loading [11], making the groove wall more susceptible to crack initiation and propagation. Under high-frequency sawing conditions, these cracks may extend laterally (increasing crack length) and extend deeper into the bone (increasing crack depth), potentially compromising implant stability and postoperative outcomes.

2.3. Chip formation and evacuation

During orthogonal cutting of cortical bone, the cutting force typically exhibits oscillations around a steady-state value, which can be decomposed into a static component and a dynamic component (Fig. 5a) [11,14]. Based on in-situ observations of bone chip formation, Wang et al. [14] attributed these fluctuations to the cyclic accumulation and release

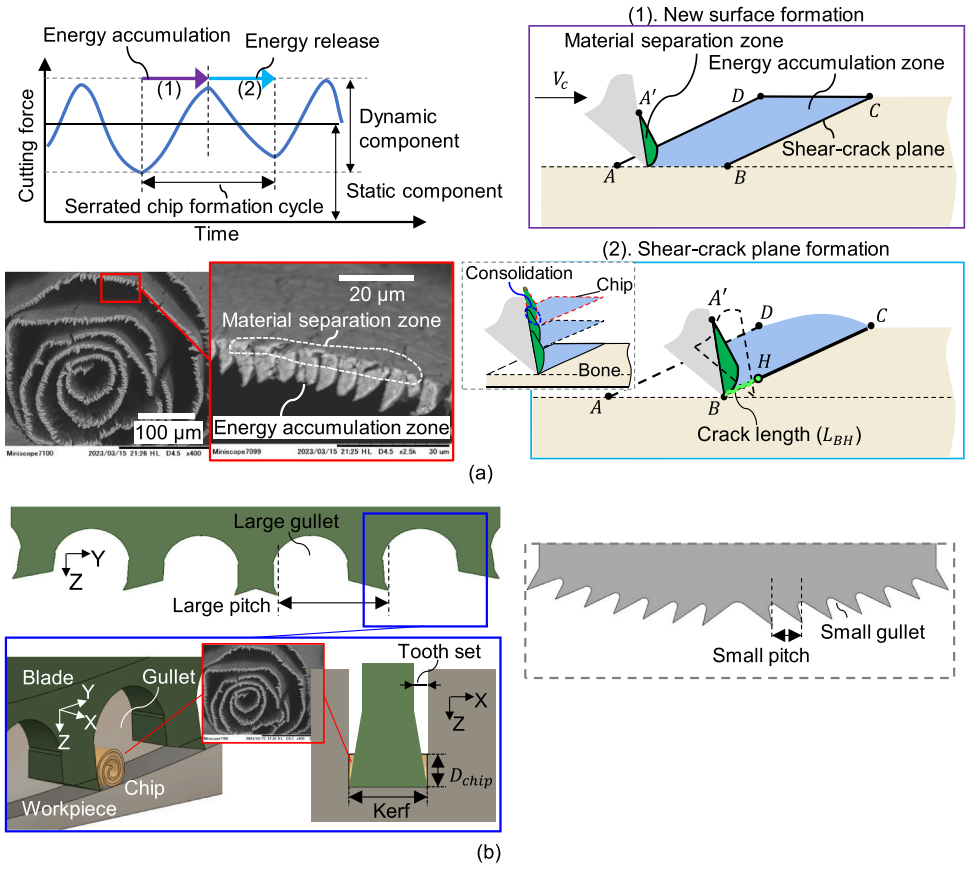

Fig. 5. Schematic of bone (a) chip formation in orthogonal cutting and (b) chip evacuation in oscillating sawing. (a) Chip formation involves two stages [14]: (1) New surface formation with plastic deformation and energy accumulation near the BC plane (force increase); (2) Shear-crack propagation, driven by the stored energy release (force decrease). The AB region corresponds to the material separation zone with chip consolidation, while the BC region is the energy accumulation zone for energy storage. Limited energy storage and short crack length increments (dL_{BH}) result in prolonged chip consolidation and continuous serrated morphologies. (b) Chip evacuation is influenced by gullet size. A small gullet limits chip storage, increasing clogging risk. A larger gullet provides more space, but spiral-shaped chips may exceed the available tooth set clearance and hinder evacuation. Typical chip diameter (D_{chip}): approximately 0.36 mm at 5 μm depth of cut and 10 mm cutting length [14]. Tooth set: 0–0.2 mm; kerf width: 0.8–2 mm.

of strain energy during the formation of serrated chips at small depths of cut (e.g., 5–20 μm). This chip formation mechanism involves two stages: (1) New surface formation, where the material undergoes plastic deformation and separates along the AB plane, accompanied by strain energy (W_{DeE}) accumulation near the shear-crack plane (BC) as cutting force increases; and (2) Shear-crack plane formation, where the stored energy is rapidly released once the energy release rate G_s along the BC plane exceeds the critical value G_c (i.e., the fracture toughness of the material), driving crack propagation and forming serrated chip segments accompanied by a drop in cutting force. The energy release rate is defined as [11,14]:

$$G_s = \frac{dW}{dA_s} = \frac{dW_{DeE}}{bdL_{BH}} \geq G_c \tag{3}$$

where A_s is the crack area in the shear-crack plane; W is the potential energy; b is the tool edge thickness; L_{BH} is the crack length along the shear-crack plane.

Despite the occurrence of shear-crack formation, complete chip separation may remain incomplete due to (i) inter-chip compressive stress, which promotes consolidation within the material separation zone (Fig. 5a), and (ii) the inherent microstructural inhomogeneity of cortical bone [14]. According to Eq. (3), the limited energy accumulation rate (dW) and short crack length increments (dL_{BH}) result in prolonged consolidation, producing serrated profile but continuous serrated morphologies.

The resulting chip morphology directly influences chip evacuation. As illustrated in Fig. 5b, bone chips are first separated from the workpiece and temporarily stored in the gullet, then discharged through the clearance formed by the tooth set. In conventional saw blades with a small pitch and high tooth number, the restricted gullet space limits chip storage, increasing the clogging risk—even when only fine, powdery or needle-like chips are formed at shallow depths of cut [30]. Conversely, blades with larger pitches allow more chip volume to accumulate. However, the continuous spiral chips commonly produced in such configurations [14,30,31] may exceed the available clearance, thereby hindering chip evacuation, also increase the clogging risk.

2.4. Temperature rise

During oscillating sawing, heat generation primarily arises from two sources: shear heat (Q_s) and ploughing heat (Q_p) [24]. The heat retained in the bone ($Q_{retained}$) consists of the entire ploughing heat and the portion of shear heat not evacuated by chips ($(1-\xi)Q_s$). Accordingly, the retained heat can be expressed as:

$$Q_{retained} = Q_p + (1-\xi)Q_s = \eta_p F_p V_c + (1-\xi)\eta_s F_s V_s \tag{4}$$

where ξ represents the chip removal efficiency, which is influenced by the gullet design and chip formation; η_p and η_s are the proportion of heat flows into the workpiece during ploughing and shearing, respectively; V_c is the cutting speeds, and V_s is the shear speeds ($V_s = V_c\cos\alpha$).

The resulting temperature rise (ΔT) during bone cutting can be estimated based on the Fourier's law of heat conduction [32]:

$$\Delta T = \frac{Q_{retained}}{k_b A} = \frac{\left(\eta_p F_p + (1-\xi)\eta_s F_s \cos\alpha\right) V_c}{k_b bh\cos\alpha} \tag{5}$$

where k_b is the thermal conductivity of bone; A is the effective contact area between tooth and bone, which is determined by the depth of cut (h), tooth thickness (b) and rake angle (α).

From the orthogonal bone cutting experiment conducted by Feldmann et al. [33], it was observed that the temperature in bone chips is higher than in the workpiece, and that tools with larger rake angles produce lower cutting temperatures. In addition, linear regression analysis between temperature rise and cutting force revealed a strong correlation for both the shear heats (Q_s) dissipated through bone chips and ploughing heat (Q_p) conducted into the workpiece, under conditions where $\xi = 1$ (i.e., ideal chip evacuation). As shown in Fig. 6, a large negative rake angle induces a dominant ploughing force (F_p) [14], which in turn generate substantial frictional heat (Q_p) near the tool–bone interface. This heat accumulates in the workpiece due to poor chip formation and the low thermal conductivity of cortical bone. In contrast, a positive rake angle promotes shear-dominated cutting ($F_s > F_p$), facilitate chip evacuation, and enhances thermal dissipation via chip evacuation.

However, even under positive rake conditions, inefficient chip evacuation (i.e., low ξ) limits the removal of shear heat, resulting in elevated temperatures. According to Eq. (5), this effect becomes particularly pronounced when high pitch density and shallow cutting depths are employed, both of which increase specific cutting forces and further intensify heat accumulation.

These findings highlight the coupled influence of rake angles, chip formation, and pitch design in governing sawing force and thermal accumulation. To overcome these limitations, the next section proposed a novel flexible-structured saw blade, which adaptively modulates the cutting depth to suppress ploughing forces while enhancing chip evacuation—offering a more effective strategy for simultaneously improving cutting performance and thermal control.

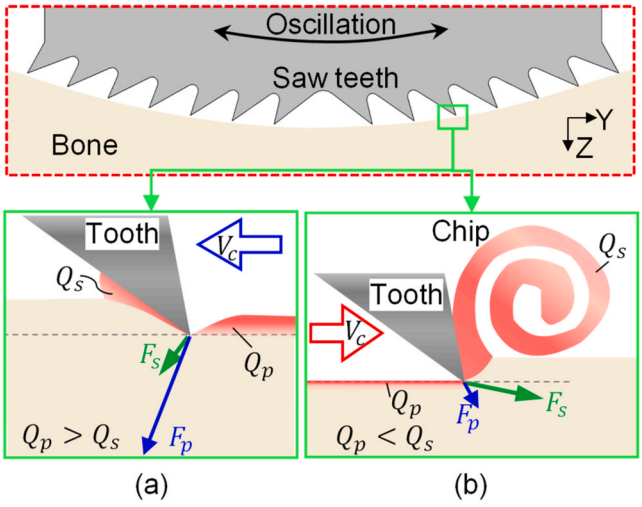

Fig. 6. Schematics of the heat generation under (a) negative and (b) positive rake angles during oscillating sawing. Q_s: heat carried away by chips due to shear force; Q_p: heat accumulated in the workpiece due to ploughing force. At negative rake angles, ploughing force dominates ($F_p > F_s$), leading to frictional heat accumulation ($Q_p > Q_s$). At positive rake angles, shear force dominates ($F_s > F_p$), promoting chip formation and heat dissipation through chip removal ($Q_s < Q_p$).

3. Design of flexible-structured oscillating saw blade

3.1. Mechanism and design of the flexure hinge structure

As mentioned in Section 1, conventional saw blade teeth are rigidly connected to the blade shank. During sawing, the resistance force on the positive rake face (R_P) is typically smaller and exhibits a larger component in the cutting direction. In contrast, the resistance force on the negative rake face (R_N) is substantially greater and exhibits a large component in the thrust direction due to ploughing.

Inspired by the reciprocating motion of shapers and planers, the proposed design, as shown in Fig. 7a, incorporates a revolute joint between the tooth and the blade shank to reduce the depth of cut under negative rake conditions. The tooth tip is offset by a distance e in the cutting direction and e' in the thrust direction from the rotation center O, enabling the tip to follow a circular arc trajectory with a radius $r = \sqrt{e^2 + e'^2}$. While cutting with the flank face (i.e., under negative rake conditions), the tooth rotates by an angle θ_N around the revolute joint, resulting in a slight upward displacement of the tip. This motion reduces the actual depth of cut ($H_N = H - \Delta h_N$), thereby decreasing the

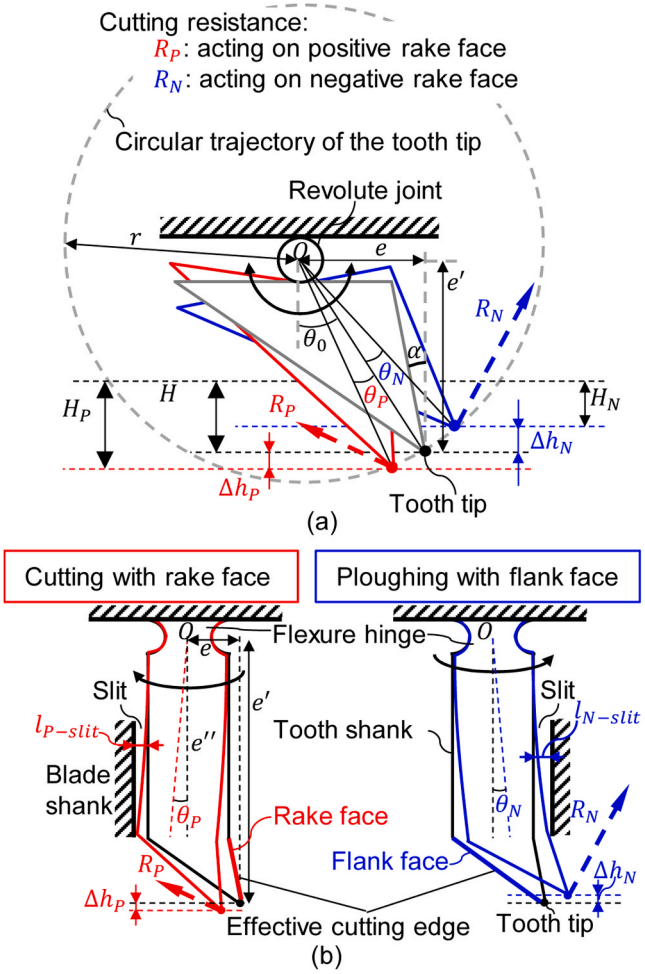

Fig. 7. Schematic of non-rigid connections between tooth and blade shank: (a) revolute joint and (b) flexure hinge joint. (R_N and R_P are the resistance generated when using the negative rake face and positive rake face, respectively; H is the ideal depth of cut; H_N and H_P are the actual depth of cut due to R_N and R_P,respectively; α is the rake angle of the rake face; θ_N and θ_P are the rotational angle of the tooth tip when using the negative rake and positive rake faces, respectively; e and e' are tooth tip offsets in cutting and thrust directions, respectively;e'' is the length of tooth shank; l_{N-slit} and l_{P-slit} are the slit widths limiting rotation under negative rake ang positive rake faces, respectively).

resistance force R_N. In contrast, when cutting with the positive rake face side, the tip rotates by an angle (θ_P), which increases the actual depth of cut ($H_P = H + \Delta h_P$) and slightly decreases the effective rake angle ($\alpha - \theta_P$), moderately increasing the resistance force R_P. The depth variations Δh_P and Δh_N resulting from these rotational motions can be expressed as

$$\Delta h_N = e' - r\cos(\theta_0 + \theta_N) = e' - r\cos\left(\arctan\frac{e}{e'} + \theta_N\right) \tag{6}$$

$$\Delta h_P = r\cos(\theta_0 - \theta_P) - e' = r\cos\left(\arctan\frac{e}{e'} - \theta_P\right) - e' \tag{7}$$

When the depth variations due to rotation (Δh_P and Δh_N) are similar, and the rotational angles (θ_P and θ_N) are small, the force increase on the positive rake face becomes negligible. This is because the specific cutting force under positive rake conditions is significantly lower than under negative rake conditions (see Fig. 2).

However, a mechanical revolute joint may introduce friction and reliability concerns at high oscillation frequencies. To overcome this limitation, a frictionless [34] and easy-to-fabricate flexure hinge was introduced as a substitute for the revolute joint (Fig. 7b). The flexure hinge is connected to the tooth tip through a cantilever-like shank, which allows for a specific range of rotational motion. This configuration is particularly suitable for bone sawing, where both the cutting depth and required rotational angle are inherently small.

To mechanically constrain the rotational angle, lateral slits are introduced on both sides of the blade shank. The maximum allowable rotational angles ($\theta_{N-\max}$, $\theta_{P-\max}$) are determined by the slit widths (l_{N-slit}, l_{P-slit}) and the effective tooth shank length (e'') as follows:

$$\begin{cases} \theta_{N-\max} = \arctan\dfrac{l_{N-slit}}{e''} \\ \theta_{P-\max} = \arctan\dfrac{l_{P-slit}}{e''} \end{cases} \tag{8}$$

As illustrated in Fig. 8a, the proposed flexible-structured tooth introduces a periodic variation in cutting depth through elastic deflection and recovery of the tooth shank. During orthogonal cutting with a positive rake, the tooth tip engages the bone surface and the shank bends, storing additional energy. Once fracture initiates and the shank rebounds, the instantaneous cutting depth is reduced, producing a wavy surface pattern and segmented chips.

Specifically, a flexible tooth structure is employed and cutting with the rake face, additional energy ($W_{DeE'}$) is accumulated through the elastic deflection of the tooth shank (Fig. 8b). Therefore, the energy release rate associated with the flexible tooth structure can be expressed by modifying Eq. (3)

$$G'_s = \frac{dW}{dA_s} = \frac{d(W_{DeE} + W_{DeE'})}{bdL'_{BH}} \geq G_c \tag{9}$$

Here, an increased energy accumulation rate (dW) under a constant fracture toughness (G_c) leads to an enlarged instantaneous crack area (dA_s), resulting in a greater crack length increment (dL'_{BH}), as shown in Fig. 8c. This facilitates more rapid chip separation from the workpiece, thereby shortening the duration of plastic deformation where chip compression and consolidation typically occur (see Fig. 5b).

Once fracture initiates ($G'_s \geq G_c$), the stored energy is rapidly released, accompanied by a sudden drop in cutting force and elastic rebound of the shank. This periodic process resembles that observed in low-frequency vibration-assisted bone drilling, where cyclic deformation facilitates discontinuous chip formation [35]. It should be noted that, due to the inherent heterogeneity of bone and the non-rigid nature of the tooth shank, the period, amplitude, and force fluctuation during cutting may vary rather than follow a uniform sinusoidal pattern as schematically illustrated in Fig. 8. Such irregularities may lead to asynchronous or delayed energy release in the shank, resulting in non-uniform chip segmentation and uneven waviness of the machined surface. This differs from actively controlled vibration-assisted cutting, where vibration frequency and amplitude are externally imposed and stabilized.

Although the flexible structure may slightly increase both the dynamic and static force components—due to enlarged vibration amplitudes, increased instantaneous cutting depth, and reduced effective rake angles—the resulting chip segmentation significantly enhances evacuation efficiency. Consequently, this mitigates the risk of chip clogging [5] and helps suppress excessive thermal accumulation during sawing.

As illustrated in Fig. 9, the slit configuration directly influences cutting depth distribution and chip removal behavior on the positive and negative rake faces.

When a slit is applied only on the negative-rake side (i.e., $l_{P-slit} = 0$, $l_{N-slit} > 0$), the cutting depth on the negative rake face is reduced, as the tooth tip is lifted under resistance. Consequently, more material is removed by the positive rake face (Fig. 9b). Conversely, with a slit only

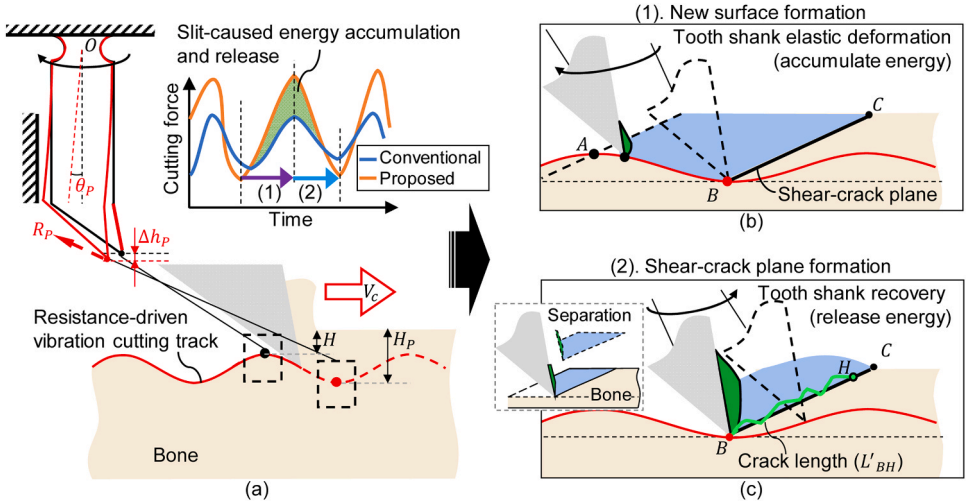

Fig. 8. Schematics of serrated chip formation with the proposed flexible-structured tooth. (a) Overview of the orthogonal cutting process. (b) New surface formation: elastic deflection of the tooth shank accumulates additional energy ($W_{DeE'}$) prior to shear-crack initiation. (c) Shear-crack plane formation: once the critical energy release rate is exceeded, the stored energy is rapidly released, increasing the crack length increment (dL'_{BH}) and accelerating chip segmentation compared to Fig. 5a. Despite slightly increased cutting forces—due to higher vibration amplitude, larger instantaneous cutting depth, and reduced effective rake angle—chip evacuation is enhanced. Due to bone heterogeneity and the non-rigid tooth structure, the period and amplitude of the cutting force waveform may vary, causing non-uniform chip segmentation and machined surface waviness—unlike externally controlled vibration-assisted cutting.

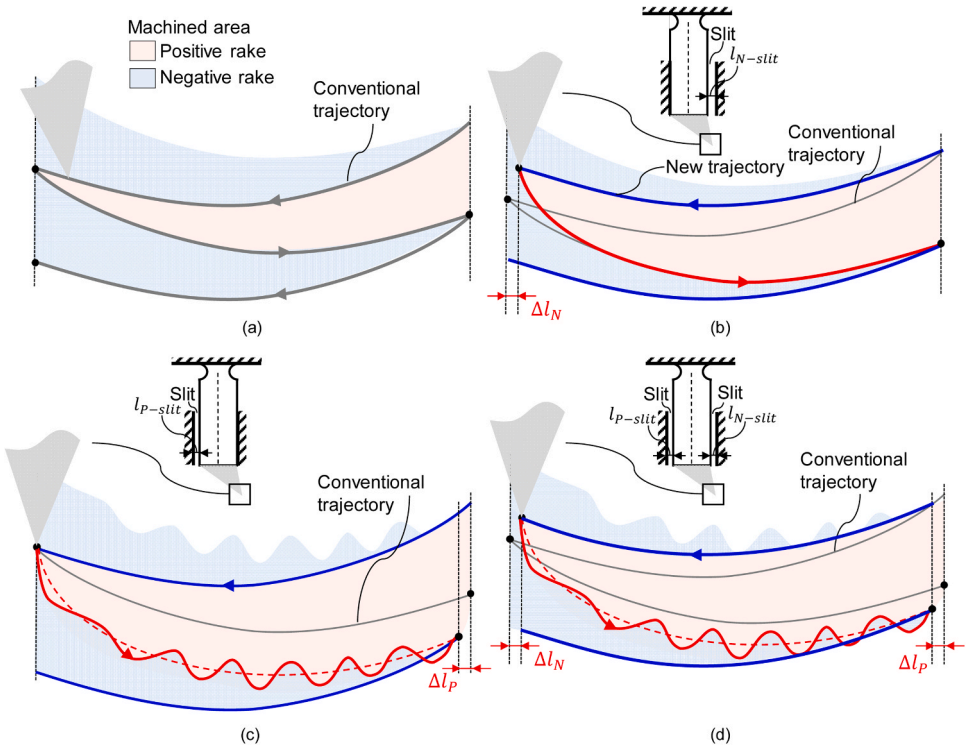

Fig. 9. Simulated distribution of the machined area for (a) conventional and (b-d) proposed saw teeth with different slit width configurations: (b) $l_{P-slit} = 0$, $l_{N-slit} > 0$: cutting depth on the negative rake face is reduced; material is primarily removed by the positive rake face. (c) $l_{P-slit} > 0$, $l_{N-slit} = 0$: elastic deformation during cutting with positive rake increases dynamic force and promotes discontinuous chip formation. (d) $l_{P-slit} > 0$, $l_{N-slit} > 0$: balanced removal between rake faces leads to improved overall cutting performance. Lateral deviations Δl_N and Δl_P result from the tooth rotation near oscillation extremes but are negligible due to the overlap of adjacent teeth.

on the positive-rake side ($l_{P-slit} > 0$, $l_{N-slit} = 0$), the tooth shank exhibits greater vibration during cutting with the positive rake face, resulting in larger dynamic force components and more discontinuous chips morphologies, which facilitates chip evacuation (Fig. 9c). When slits are applied on both sides ($l_{P-slit} > 0$, $l_{N-slit} > 0$), the cutting forces and chip evacuation characteristics are balanced between the two rake faces, leading to improved overall cutting performance (Fig. 9d). Although slight lateral deviations (Δl_N and Δl_P) may occur near the oscillation extremes due to tooth rotation, these uncut areas are typically removed by adjacent teeth in subsequent oscillation cycles and therefore have negligible impact on surface quality.

Based on the above analysis, the proposed flexible tooth structure demonstrates strong potential to suppress ploughing effects while promoting the formation of discontinuous chips, thereby enhancing chip evacuation effectively.

3.2. Fabrication of the flexible-structured saw blade prototype

To implement the proposed flexible-structured concept, a novel bone saw blade was designed and fabricated, consisting of a blade shank with five embedded saw teeth (Fig. 10). Given the reduced cutting force per tooth expected from the compliant design, the total number of teeth was halved compared to conventional blades, thereby enlarging the gullet space and improving chip evacuation (Fig. 10a,b). Considering the orientation of the tooth tips and the conventional saw blade shape mentioned in Fig. 1b, the central tooth was designed with a dual-tip structure, while the remaining teeth were single-tipped to maintain balance and ensure directional cutting efficiency.

As shown in Fig. 10c, each saw tooth consists of five distinct sections: (1) tooth tip, which performs the actual cutting; (2) tooth head, which is wider to mechanically support the tooth tip; (3) tooth shank and (4) flexure hinge, which together provide structural compliance and enable controlled deflection of the tooth tip; (5) tooth root, which is interference-fitted into the blade shank within a designated fitting region (Fig. 10a,b). The fitted tooth shank incorporates two L-shaped narrow slits on either side of the blade shank ridge, allowing for limited deflection of the saw tooth shank and reducing the risk of breakage due to excessive deformation or force. In addition, to prevent bone chips from entering and clogging the slits, the slits were filled with an elastic material (Fig. 10b), such as silicone rubber, which is widely used in medical-grade implantable devices due to its excellent biocompatibility, chemical stability, and physical flexibility [36]. The main parameters of the prototype design are summarized in Table 1. The positive rake angle (α) was set as 20° to reduce the forces, while the lip angle (δ) was set to 50° to preserve tip strength. The tooth set (Δb) was defined as 0.2 mm to facilitate chip evacuation (Fig. 10d).

α: rake angle; δ: lip angle; ω: angle between the adjacent teeth; H_T, H_H, H_S, H_F, H_R: height of tooth tip, tooth head, tooth shank, flexure hinge, and tooth root, respectively; W_H, W_S, W_F, W_R: width of tooth head, tooth shank, flexure hinge, and tooth root, respectively; d: diameter of tooth root; b, Δb: thickness of tooth tip and offset value; R, W: oscillating radius and blade width.

Both the tooth and blade shank components were fabricated from a stainless-steel plate (JIS SUS440C) with dimensions of 100 mm in length, 25 mm in width, and 1.64 mm in thickness. The profiles of the components were shaped using wire electrical discharge machining (EDM). Subsequently, the fabricated teeth were assembled into the blade shank via interference fitting using a lever press. The assembled blade was then immersed in a pre-mixed, addition-cure silicone rubber (Ecoflex 00–10, SMOOTH-ON). To ensure complete filling of the slits and eliminate air bubbles, the assembly was placed in a vacuum chamber for 30 min. After degassing, the excess silicone was trimmed, and the structure was thermally cured at 70 °C to complete the fabrication process.

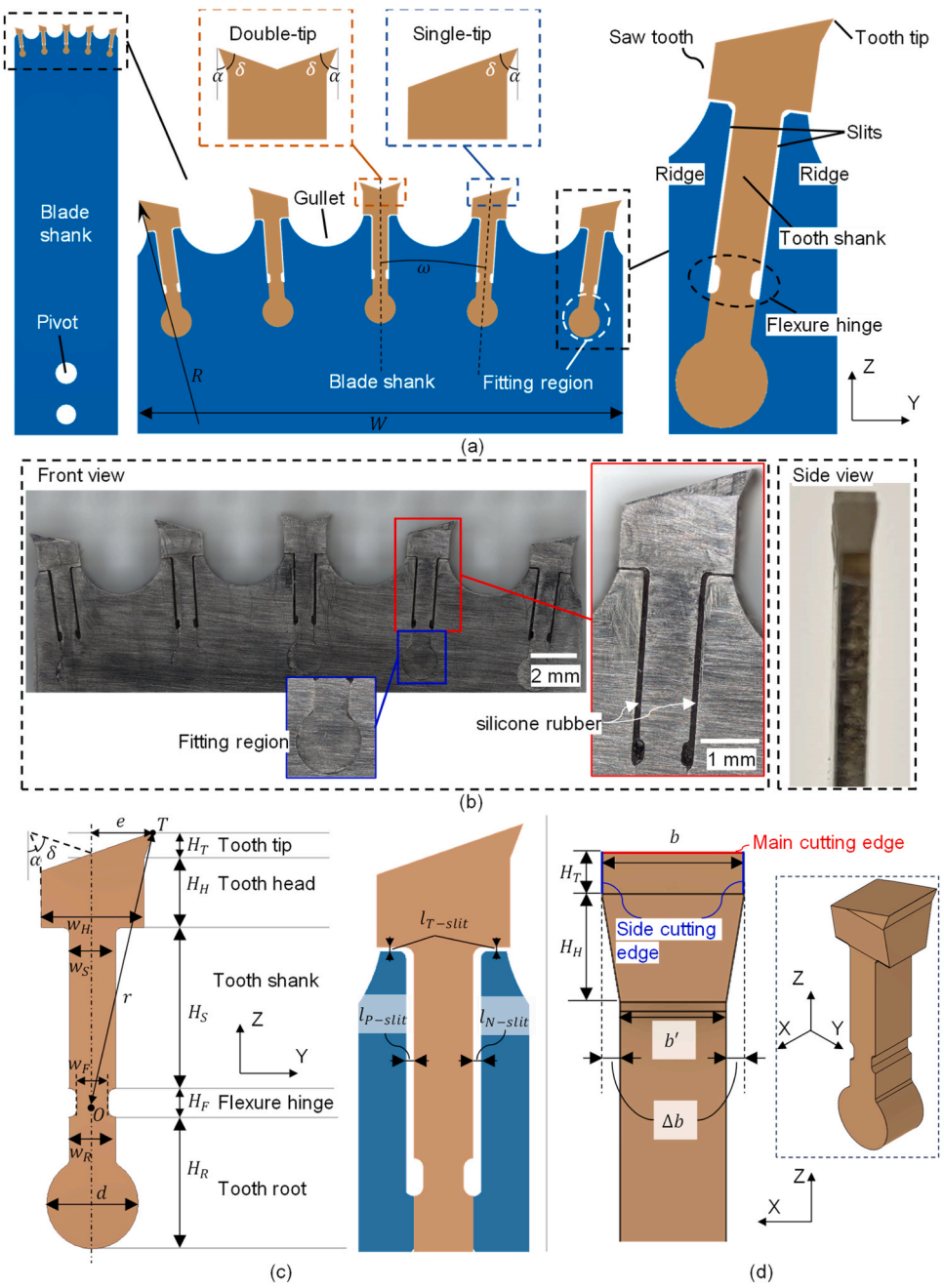

Fig. 10. Design and fabricated prototype of the flexure-based oscillating saw blade. (a) Schematic geometry of the blade with five embedded teeth; (b) prototype of the proposed saw blade; (c) front view and (d) side view of saw tooth component. (α and δ is the rake angle and lip angle of tooth tip, respectively; w and H are the widths and height of each component of the saw tooth, respectively; l_{T-slit} is the width of the slit between tooth head and ridge of the blade shank; R is the oscillating radius of the tooth tip; ω is pitch angle between the adjacent teeth; b and b' are the thickness of tooth cutting edge and tooth shank, respectively; Δb is the tooth set distance.).

Table 1
Design parameters of the saw blade prototype.

α, δ, ω(°)	r, e (mm)	H_T, H_H, H_S, H_F, H_R(mm)	W_H, W_S (W_R), W_F, d(mm)	b, Δb(mm)	l_{T-slit}, l_{P-slit}, l_{N-slit} (mm)	R, W(mm)
20, 50, 3.87	5, 1.08	0.47, 1.2, 2.83, 0.5, 2.32	1.8, 0.84, 0.59, 1.64	1.6, 0.2	0.04, 0.1, 0.1	84.5, 25

4. Experimental verification

4.1. Experimental setup and procedure

As shown in Fig. 11, comparison experiments were conducted using a setup based on a machining center (AJV-18, Yamazaki Mazak). A custom-built oscillating motion unit (oscillation angle: ±2.5°, maximum oscillation frequency: 100 Hz) was mounted on the X-axis table of the machining center. Sawing forces were measured with a 3-component force sensor (9327 C, Kistler) and recorded with a data logger (NR-

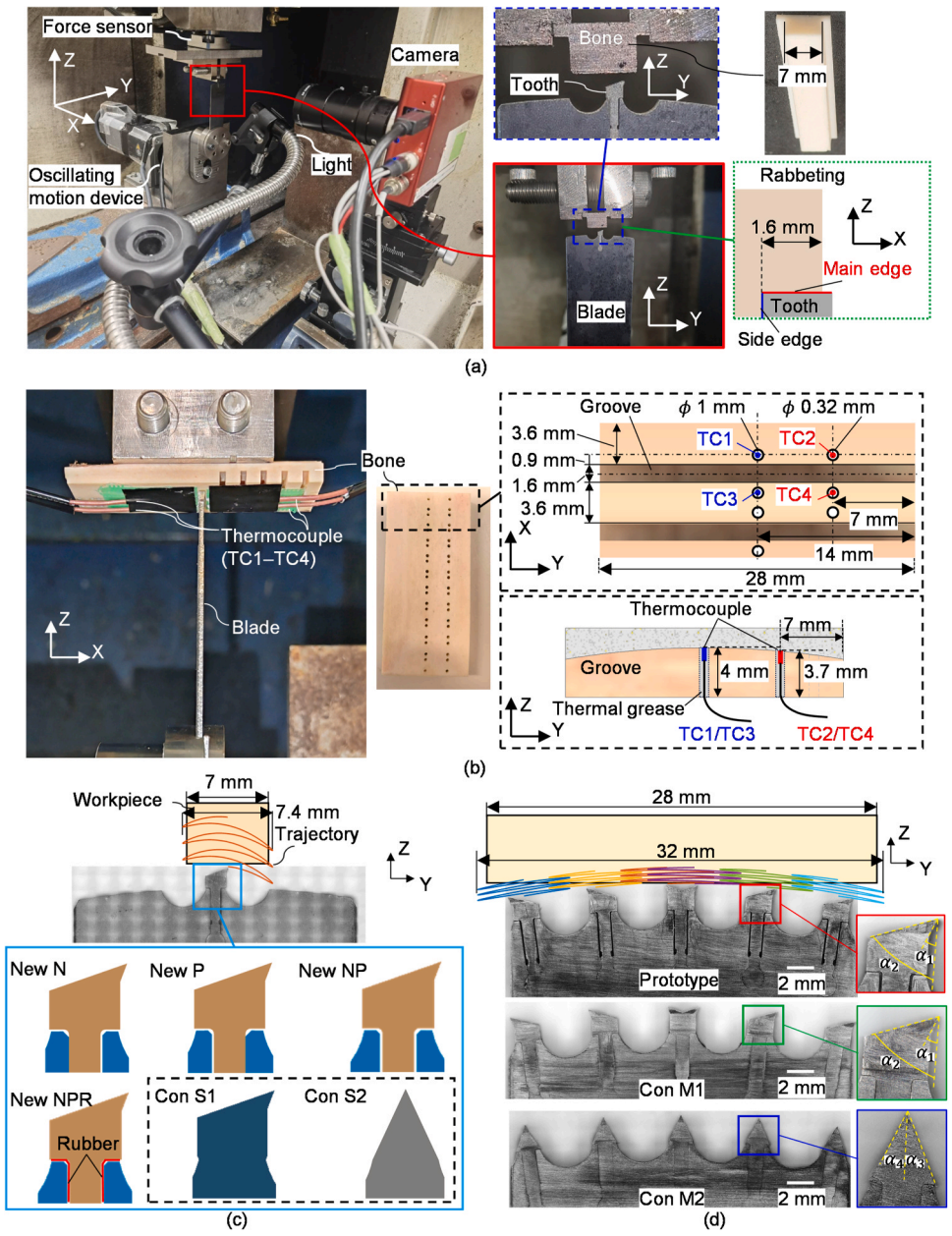

Fig. 11. Experimental set up for (a) single-tooth sawing and (b) multi-tooth sawing. Different workpiece widths setting and saw blades for (c) single-tooth and (d) multi-tooth sawing. Proposed blades in single-tooth sawing experiment: New N (l_{P-slit}: 0, l_{N-slit}:0.1 mm); New P (l_{P-slit}: 0.1 mm, l_{N-slit}:0); New NP (l_{P-slit}: 0.1 mm, l_{N-slit}:0.1 mm, without rubber in the slits); New NPR (with rubber in the slits of New NP type blade). Conventional blades in single-tooth sawing experiment: Con S1 (same tooth tip shape with the proposed blades, i.e., α_1: 20°, α_2: −70°), Con S2 (same negative rake angle in both directions, i.e., $\alpha_3 = \alpha_4 = -25°$). In the multi-tooth sawing experiment, two conventional blades (Con M1 and Con M2) were used as rigid-body controls, having the same tooth offset as the prototype but with a slit width of zero, thereby eliminating structural flexibility. Con M1 featured the same tooth tip geometry as the prototype, while Con M2 adopted the same tooth shape as Con S2.

600, Keyence) at a sampling frequency of 10 kHz.

To investigate both the sawing process and the effectiveness of the proposed structure, single-tooth and multi-tooth sawing experiments were conducted separately. A high-speed camera (HAS-EF, DITECT) was used to observe the sawing process in single-tooth sawing experiment through rabbeting (sawing a groove along the edge of the bone [3], kerf width: 1.6 mm) (Fig. 11a). Four T-type thermocouples (D-TF5, HAYASHI DENKO) were used to measure the temperature rise in multi-tooth sawing experiments (Fig. 11b). The workpieces of cortical bone were taken from the mid-diaphysis of fresh bovine femurs, and the cutting direction was chosen across the osteon direction to mimic clinical sawing conditions [3]. For high-speed imaging, the observed surface was blackened in advance with a black marker to improve visual contrast (Fig. 11a).

In the single-tooth sawing experiments (Fig. 11a,c), six types of single-tooth blades were tested: New N, New P, New NP, New NPR, Con S1, Con S2. Rabbeting was performed on a bovine cortical bone with a width of 7 mm, corresponding to the tooth tip oscillation range of 7.4 mm. Each blade was manufactured according to the method described in Section 3.2 (blade thickness: 1.61 mm, flat tooth shape (i.e., zero offset)). To avoid contact between the blade shank and workpiece, the feed distance each time was set as 1 mm. New N, New P, and New NP represent the proposed saw tooth structures with different slit width configurations (see Fig. 9b-d; with slit widths of 0 or 0.1 mm), consistent

with the prototype structure proposed in Section 3.2 (excluding offset-related parameters). New NPR is with silicone rubber in the slits of New NP. Con S1 and Con S2 are conventional saw teeth with positive (20°) and negative (−25°) rake angles, respectively. The cutting conditions for the single-tooth sawing were listed in Table 2. To clearly capture cutting behavior, including video and force trends within each cycle, the oscillation frequency was set to 5 Hz, and the depth per oscillation cycle was varied (5, 10, 20, 30 μm) by adjusting the corresponding feed speed. In addition, prolonged sawing tests were performed using additional fabricated blades (New NPR, Con S1, and Con S2) to evaluate tooth wear. These were conducted at an oscillation frequency of 50 Hz, with a depth per cycle of 20 μm and a total feed distance of 30 mm. A higher frequency (e.g., 100 Hz) was avoided due to severe X-direction vibration caused by rabbeting, where only one side of the blade contacts the workpiece.

In the multi-tooth sawing experiments (Fig. 11b,d), the proposed prototype blade (Prototype) mentioned in Section 3.2 were compared with another two conventional blades (Con M1 and Con M2) to evaluate their effectiveness in suppressing sawing force and temperature rise. To avoid impact force at the oscillation extremes, the workpiece width was set as 28 mm, which is less than the oscillation range (32 mm for Prototype and Con M1, 30 mm for Con M2). Pre-drilled holes (1 mm diameter) were positioned 0.9 mm from both sides of the kerf to insert thermocouples (TC1–TC4), yielding a minimum distance of 0.4 mm from the kerf surface. TC1 and TC3 were positioned at the center of the workpiece width; TC2 and TC4 were placed 7 mm away from the center, allowing temperature variations monitoring in both the center and side regions. Considering the feed depth of 4 mm and the formation of an arc-shaped groove (radius matching the oscillating radius), the hole depths were set to 4 mm and 3.7 mm, respectively. To ensure adequate thermal conduction, the holes were filled with thermal grease [37]. Additionally, each cutting groove was spaced 3.6 mm apart to prevent thermal and mechanical damage to adjacent grooves [6]. The cutting conditions for the multi-tooth sawing are summarized in Table 3. To simulate clinical conditions, the oscillation frequency was set to 100 Hz with a feed speed of 2 mm/s. A low-vacuum scanning electron microscope (SEM; TM3000, HITACHI, operated at 15 kV in low-vacuum mode) was used to observe bone chip morphologies and surface cracks. A digital microscope with integrated laser-induced breakdown spectroscopy (VHX-EA300, Keyence; with 100 ×–1000 × magnification) was employed to examine tooth wear, chip morphologies and perform elemental analysis. A 3D laser scanning microscope (VK-X200, Keyence; with 200 ×–3000 × magnification) was used to characterize surface topography.

4.2. Data processing

The sawing force is inherently time-varying due to the fluctuating instantaneous cutting depth and cutting speed. In addition, the low-frequency structural vibration introduced by the proposed flexure-based tooth design may further influence the force response. Therefore, the measured force signal was decomposed into two components for analysis: a static force component, representing the low-frequency trend (also referred to as trend force); and a dynamic force component, capturing high-frequency oscillations (also referred to as vibration force) induced by intermittent tool–material interactions.

As shown in Fig. 12, the raw force signal data were first processed using a 4th-order Butterworth band-stop filter (450–550 Hz) to eliminate environmental noise. The denoised signal was then separated into low- and high-frequency components using low-pass and high-pass filters, corresponding to the trend force and vibration force, respectively. The cutoff frequencies were empirically selected based on the oscillation frequency to ensure accurate component separation without distortion. Specifically, a 200 Hz cutoff was applied under the low-frequency oscillation condition (5 Hz); and a 400 Hz cutoff was applied for the 50 Hz and 100 Hz oscillation conditions. These filter settings allowed for the preservation of low-frequency fluctuations in the trend force while retaining high-frequency oscillations relevant to vibration force analysis.

Table 2
Experimental conditions for single-tooth sawing.

Workpiece materials	Bovine cortical bone, width: 7 mm, thickness: 6 mm
Oscillation range	7.4 mm
Oscillation frequency	5 Hz; Wear test: 50 Hz
Feed speed	0.05, 0.1, 0.2, 0.3 mm/s; Wear test: 2 mm/s
Depth per oscillation cycle	5, 10, 20, 30 μm; Wear test: 20 μm
Feed distance	1 mm; Wear test: 1 mm × 30 feed cycles

Table 3
Experimental conditions for multi-tooth sawing.

Workpiece materials	Bovine cortical bone, width: 28 mm, thickness: 6 mm
Oscillation range	32 mm (Prototype, Con M1); 30 mm (Con M2)
Oscillation frequency	100 Hz
Feed speed	2 mm/s
Depth per oscillation cycle	20 μm
Feed distance	4 mm
Environmental temperature	22 °C

5. Results and discussion

5.1. Single-tooth sawing

5.1.1. Single-tooth sawing force and process characteristics

Fig. 13 shows the comparison of sawing force between the proposed structure (New N) and two conventional blades (Con S1 and Con S2). Due to the same positive rake angle ($\alpha_1 = 20°$) and the absence of structural flexibility on the flank face side ($l_{P-slit} = 0$), New N and Con S1 exhibited similar force trends when cutting with the positive rake face. However, on the negative-rake-face side ($\alpha_2 = -70°$), New N generated significantly lower forces than Con S1 (Fig. 13a,b). In addition, the larger difference between the mean and maximum force values on the negative rake face indicates greater variability in instantaneous cutting depth (Fig. 1a). In contrast, the smaller difference observed on the positive rake face may be attributed to the elastic recovery of the workpiece, which reduces fluctuations in actual cutting depth during negative-rake-face engagement, as discussed in Wang et al. [22]. In the case of Con S2, the use of a symmetric negative rake angle ($\alpha_3 = \alpha_4 = -25°$) generates a similar variation in both cutting directions (Fig. 13c). Moreover, its feed-direction force component (Fz) was smaller than that of Con S1, indicating that a larger positive rake face in a rigid structure does not sufficiently reduce the overall oscillating sawing force.

As shown in Fig. 13d, New N achieved substantial force reduction under negative rake angle conditions. Specifically, compared to Con S1 at α_2, New N reduced force by 61–78 % in the oscillation direction (Fy) and 73–86 % in the feed direction (Fz); compared to Con S2 at α_4, the reductions were 72–88 % (Fy) and 57–90 % (Fz), respectively. By contrast, the force reduction ratios between a positive rake angle (α_1) and a negative rake angle (α_3) in a rigid conventional tooth (Con S1 vs. Con S2) was limited: 8–33 % for Fy, 48–69 % for Fz. These results underscore that rake angle modification alone is insufficient, while the integration of structural flexibility enables more effective reduction of oscillating sawing forces, particularly under unfavorable (negative rake) engagement conditions.

Fig. 14 shows the trend force and vibration force components associated with different configurations of the newly designed single-tooth saw blades. For New N (Figs. 13 and 14a), which features zero slit width on the flank face side, the vibration force remained low, comparable to that of conventional blades. In contrast, introducing non-zero slit widths on the flank-face side led to varying degrees of the vibration in New P (Fig. 14b), New NP (Fig. 14c) and New NPR (Fig. 14d).

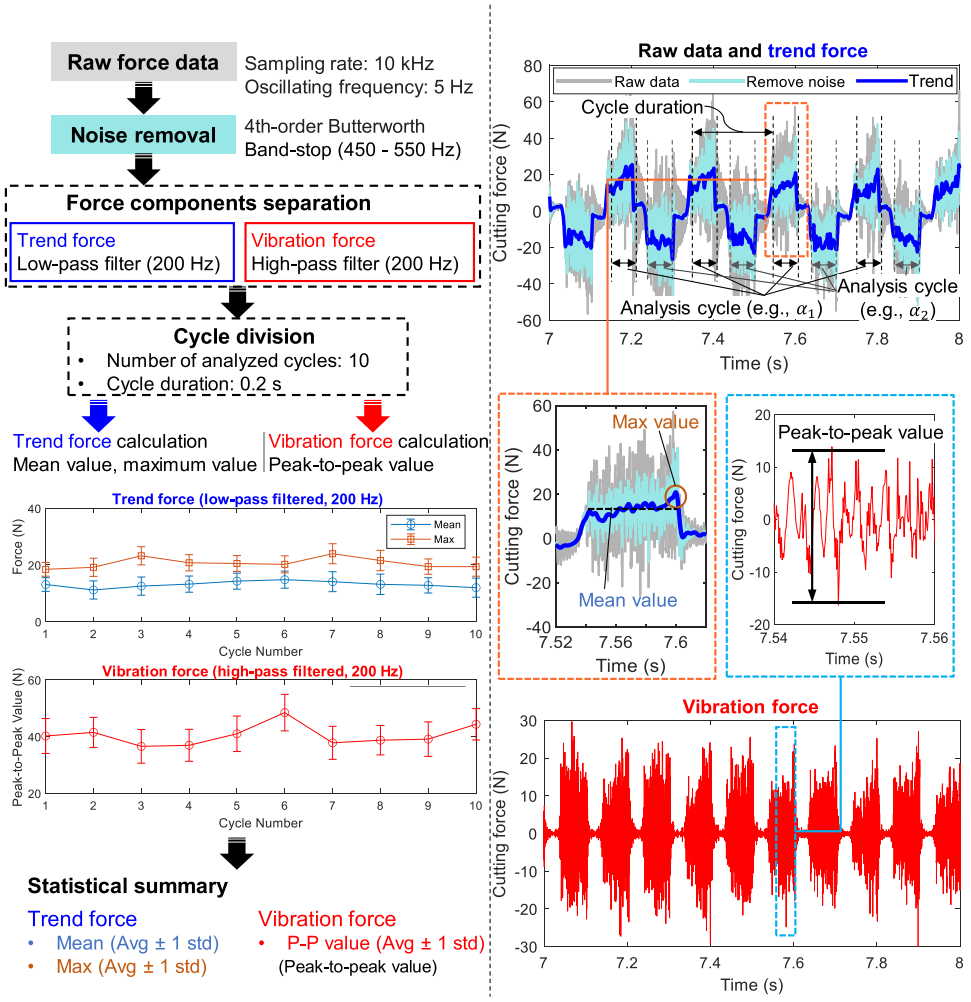

Fig. 12. Data processing workflow for cutting force analysis. The example shown corresponds to an oscillation frequency of 5 Hz. The raw force data were first filtered to remove environmental noise, then separated into low-frequency trend force and high-frequency vibration force using 4th-order Butterworth filters (cutoff: 200 Hz). Trend force was quantified by mean and maximum values within each analysis cycle, while vibration force was characterized by its peak-to-peak value. Error bars (shown on the positive side only) represent ±1 standard deviation. Number of analyzed cycles: 10.

When cutting with the positive rake face, Fz exceeded Fy, which can be ascribed to periodic compressive interactions between the flank face and the workpiece induced by vibration-assisted contact [35]. Among the configurations, New NP, which incorporated slits on both sides, produced the largest vibration amplitude and trend force (Fig. 14c). In comparison, New NPR, which included silicone rubber embedded in the slits as a damping material, generated the lowest trend and vibration forces (Fig. 14d), outperforming both New P (Fig. 14b) and New NP (Fig. 14c) in terms of dynamic force suppression and overall force reduction.

These large vibration forces resulted from passive vibration-assisted cutting that occurred during the sawing process, as illustrated in Fig. 15 and Supplementary Video 1. In the case of conventional blades (Con S1 and Con S2, Fig. 15e,f) and New N, which featured zero-slit width on the flank face (Fig. 15a), continuous and spiral-like bone chips were observed, consistent with the SEM morphology shown in Fig. 15g. In contrast, the use of New P (Fig. 15b), New NP (Fig. 15c), and New NPR (Fig. 15d) resulted in the formation of needle-like, fragmented chips, which corresponded to the morphology shown in Fig. 15h. The formation of these fragmented chips is attributed to the energy accumulation and release behavior of the new flexible tooth structures, as previously analyzed in Section 3.1. Specifically, the stored energy was rapidly released during cutting, even causing a transient drop in force to zero, which further promoted chip segmentation (Fig. 16, Supplementary Video 1).

Among all tested designs, the New NPR blade structure demonstrated the most favorable performance by generating needle-like chips and significantly reducing both cutting and vibration forces. It was therefore selected as the structural basis for the prototype blade (i.e., Prototype).

5.1.2. *Single-tooth tip wear behavior*

In the wear test with a total feed of 30 mm, noticeable differences in tooth tip recession, including tip shape deformation and rounded edge wear, were observed among the three blades (Fig. 17). Owing to the large negative rake angle on the flank face, both New NPR (Fig. 17a,d) and Con S1 (Fig. 17b,e) exhibited more pronounced deformation than Con S2 (Fig. 17c,f). However, the edge radius of New NPR remained unchanged, indicating minimal wear. The observed deformation in New NPR is primarily attributed to the use of a positive rake angle combined with low-frequency vibration, which increased the intermittent contact between the flank face and the workpiece [35], thereby inducing a larger thrust force, mainly in feed direction, as feed distance increased (Fig. 17g). Despite this deformation, the cutting force did not increase significantly, which can be attributed to the negligible change in edge radius and the increased effective rake angle after deformation (Fig. 17a, d). In contrast, Con S1 exhibited both deformation and considerable edge wear, resulting in a larger edge radius. As the worn flank face re-engaged workpiece, a substantial increase in cutting force was

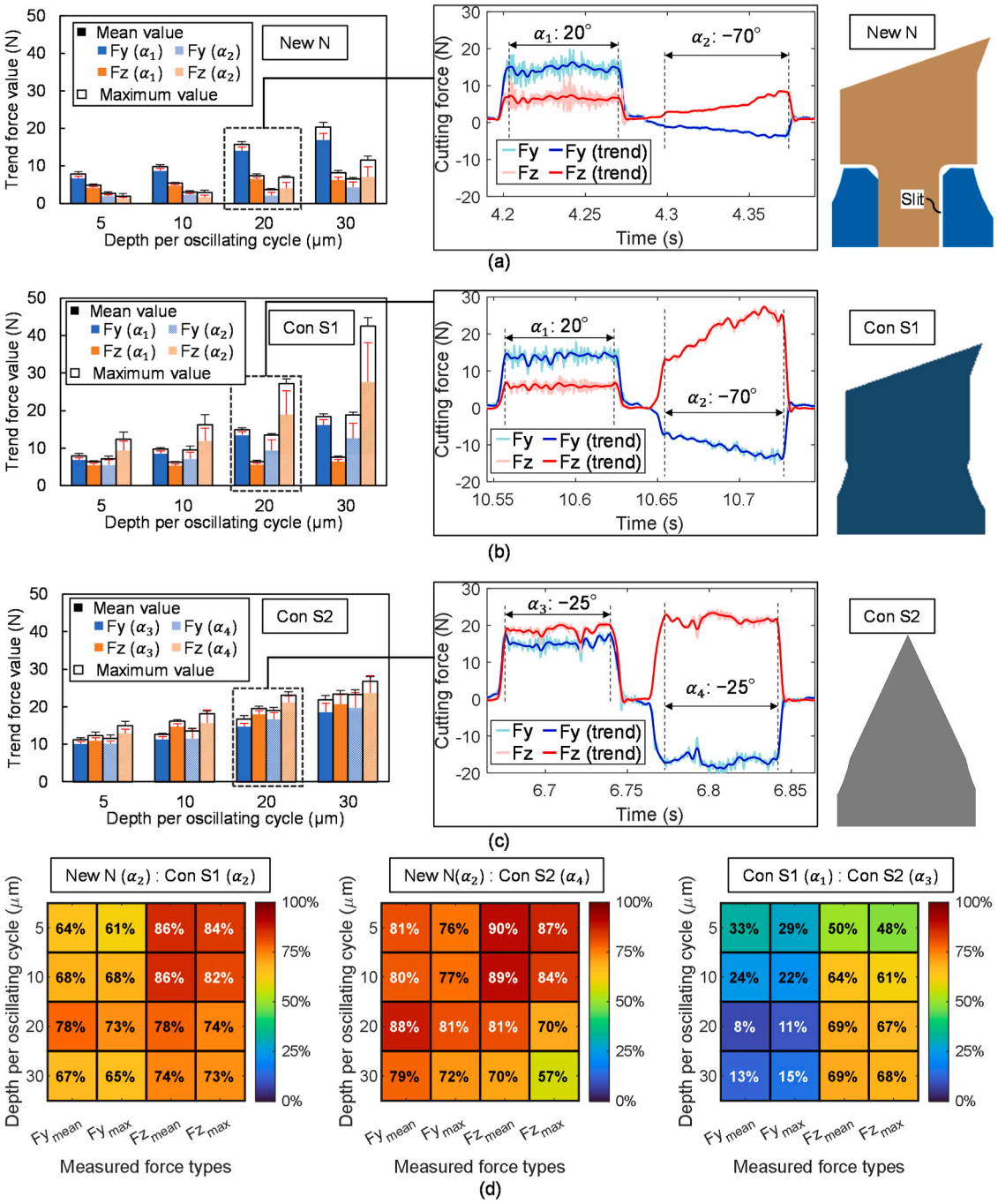

Fig. 13. Measured cutting force in single-tooth sawing experiment by using different blades: (a) New N, (b) Con S1, and (c) Con S2. Force components in the oscillation direction (Fy, primarily cutting force) and the feed direction (Fz, primarily thrust force) were extracted from raw signals and quantified by their mean and maximum values. Error bars (shown on the positive side only) represent ±1 standard deviation. (d) Reduction ratios of mean and maximum forces between blades, highlighting the effectiveness of the proposed flexure-structured teeth in reducing sawing forces.

observed, attributable to a severe ploughing effect. Although Con S2 (Fig. 17c,f,i) exhibited lower and more stable forces than Con S1, it showed more severe wear, potentially due to sustained friction and ploughing forces acting on both negative rake faces throughout the sawing process.

As the oscillation frequency increased from 5 Hz to 50 Hz, the difference between the maximum and mean cutting forces within each half cycle becomes more pronounced, even during the first feed cycle when recession was minimal (50 Hz: Fig. 17g-I; 5 Hz: Figs. 13b,c and 14a). This effect is particularly notable in Con S1 (Fig. 17h), where the higher cutting speed reduced the fracture toughness of cortical bone, thereby lowering the mean force [14]. Meanwhile, increased tool-material interaction instability at higher frequencies led to both elevated vibration amplitude and maximum forces in the conventional blades (Con S1 and Con S2). As a result, the distinction in vibration force between the conventional and proposed blades diminished under high-frequency sawing conditions.

5.2. Multi-tooth sawing

5.2.1. Multi-tooth sawing force analysis

As shown in Fig. 18, the proposed prototype blade (Prototype)

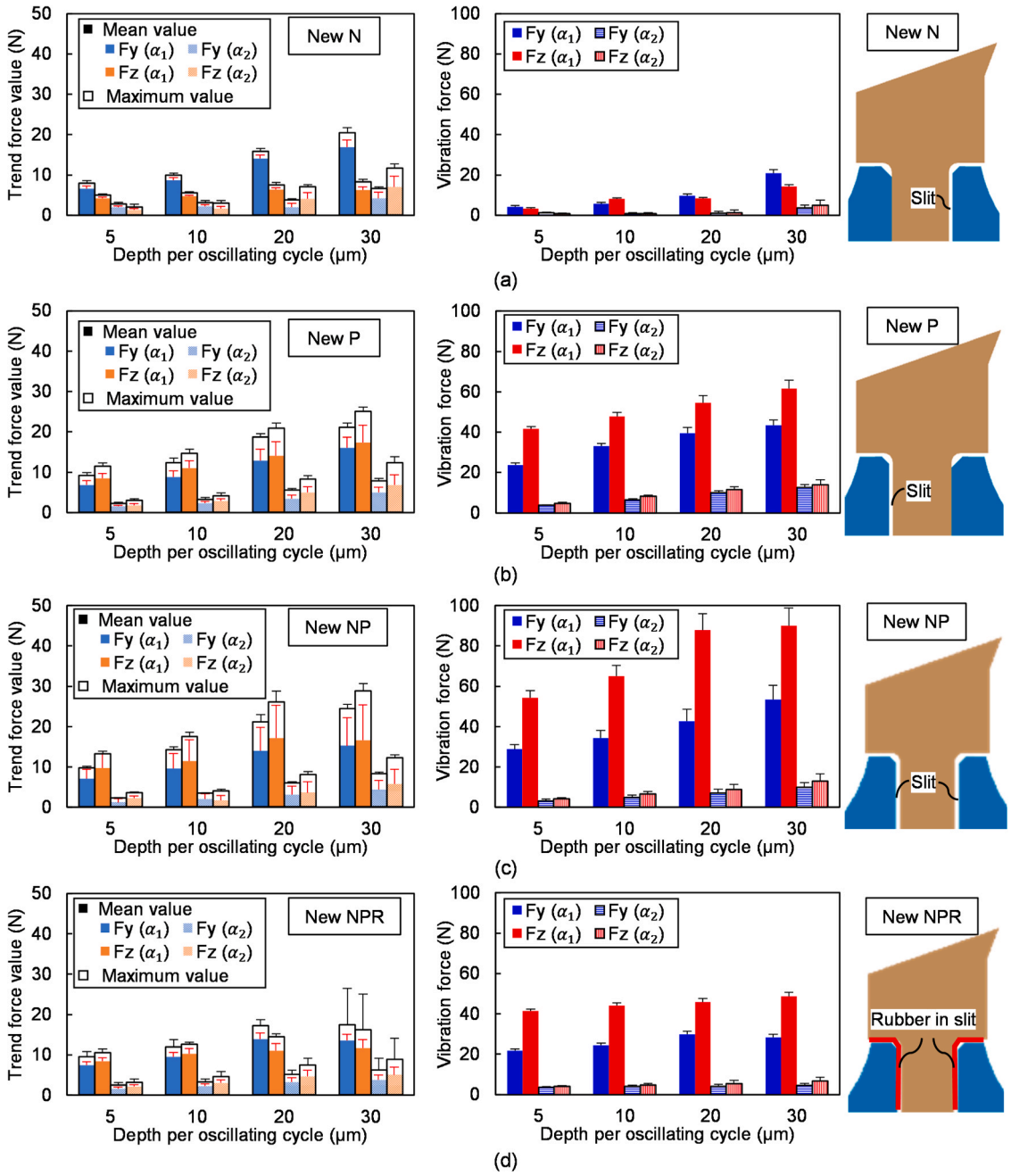

Fig. 14. Trend and vibration forces by using different types of new single-tooth saw blades: (a) New N, (b) New P, (c) New NP, and (d) New NPR. Force components (Fy and Fz) were extracted and decomposed as described in Fig. 12. Error bars (shown on the positive side only) represent ±1 standard deviation.

generated lower cutting forces than the conventional saw blades Con M1 and Con M2. In Fig. 18a–c, the mean values of the trend forces show that Prototype reduced Fy by 36.7 % and Fz by 56.4 % relative to Con M1, and Fy by 24 % and Fz by 38.1 % relative to Con M2. For the conventional blades, Fz exceeded Fy, with mean Fz/Fy ratios of 1.66 (Con M1) and 1.40 (Con M2). In contrast, Prototype significantly reduced feed-direction force (Fz), achieving a mean Fz/Fy ratio of 1.14, which may enhance tactile feedback and reduce fatigue for the surgeon or robotic system during prolonged operations.

Fig. 18d–f shows the trend force variations within a single oscillation cycle. As discussed in Section 2.1 and Fig. 3, the cycle starts at the leftmost oscillation position ($t = t_0$, Fig. 18g). Both Fy and Fz increase as the blade oscillating to the right, reaching their peaks when the instantaneous cutting depth of the tooth tip reaches its maximum at t_1, especially in the trend Fz. As the blade is oscillated to the rightmost extreme ($t = 3t_0$), Fy decreases to zero, and Fz drops to a valley value due to the change in cutting direction. A similar pattern was observed in the second half of the cycle ($3t_0 < t \leq 5t_0$). Notably, the valley values of trend Fz vary across the three blades. Although the peak-to-valley amplitudes were similar, the lower peak force in Prototype results in its valley value approaching zero (Fig. 18d). In contrast, Con M1 (Fig. 18e) showed the highest valley force at approximately 69 N, followed by Con M2 (Fig. 18f) with a valley value around 37 N. These results indicate that Con M1 consistently experiences high forces, whereas the prototype allows periodic force reduction near the oscillation extremes. This behavior can be attributed to the small thrust forces generated by the prototype's teeth (see Section 5.1.1), and from the cutting force on the right-side tooth tips producing a feed-opposing force component, further reducing Fz. Additionally, the outermost tooth tip moving out of the workpiece near the extremes also contributes to force reduction

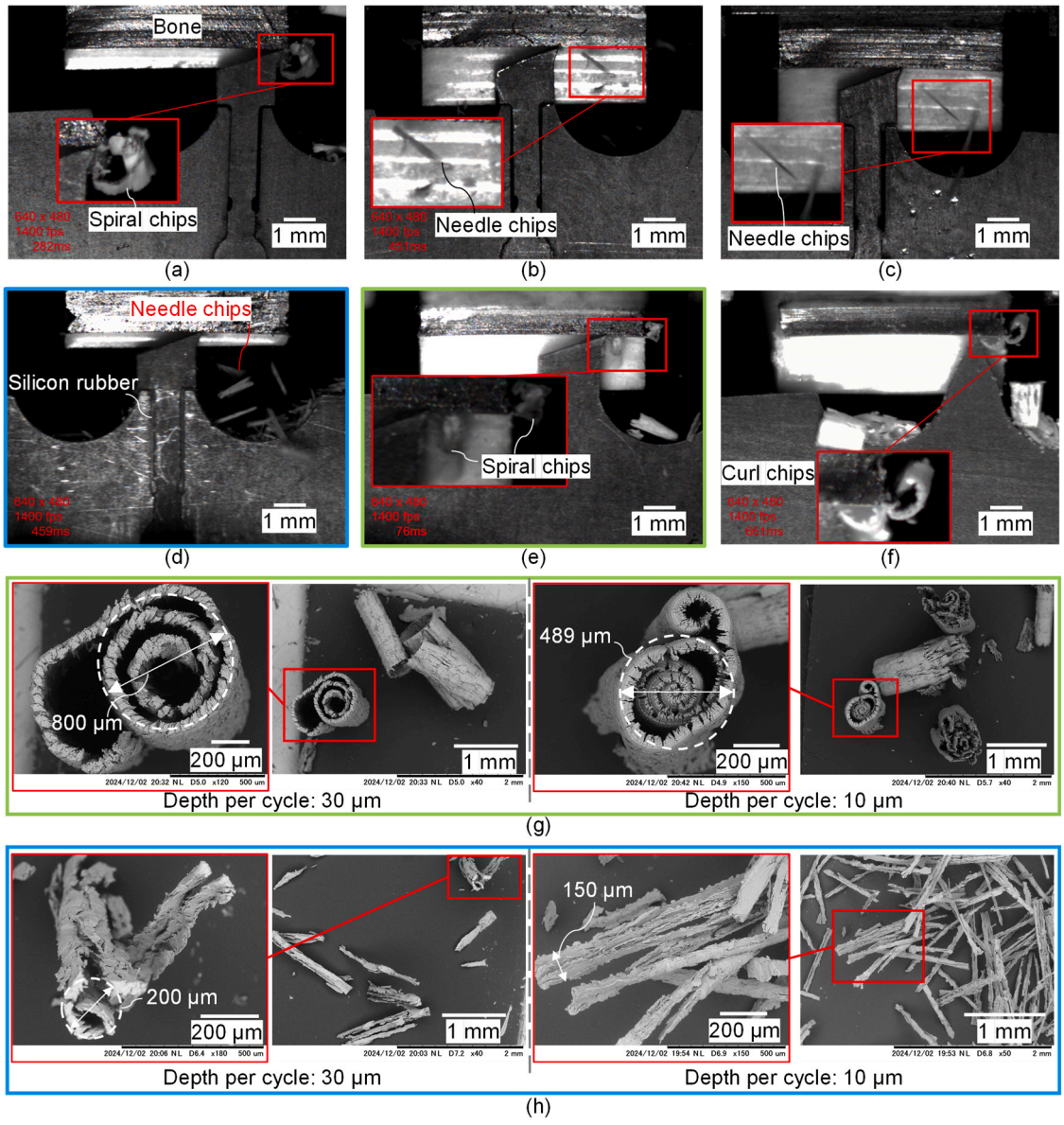

Fig. 15. Different sawing processes with chip formation (depth per cycle: 20 μm): (a) New N, (b) New P, (c) New NP, (d) New NPR, (e) Con S1, (f) Con S2. Images were extracted from high-speed recordings presented in Supplementary Video 1. Corresponding SEM images of the chip morphologies (depth per cycle: 30 μm, 10 μm): (g) Con S1, (h) New NPR. Spiral chips were typically formed with rigid or zero-slit blades, while fragmented, needle-like chips appeared under flexible configurations.

(Fig. 18g). In contrast, in Con M1, the large negative rakes on the left-side teeth produce large ploughing forces, sustaining a high trend Fz even at valley points (Fig. 18h).

On the other hand, the denoised force data indicates that, despite passive low-frequency vibrations induced by its flexible structure, the prototype still exhibited lower cutting forces (Fig. 18a) than the conventional blades, especially Con M1 (Fig. 18b), despite sharing the same tooth tip geometry. The vibration force components observed in the conventional blades were amplified by the high oscillation frequency, which increased the system's susceptibility to vibration, as well as by the complex interactions between teeth and bone. For example, in Con M1, although the teeth are symmetrically distributed on both sides of the blade, their functional behavior during sawing is asymmetric: while one side engages the bone with the positive rake face, the other simultaneously experiences ploughing via the flank face. This functional asymmetry causes uneven loading, which contributes to greater vibration amplitudes and instability in cutting forces (Fig. 18h).

5.2.2. *Temperature rise in multi-tooth sawing*

Consistent with the analysis in Section 2.4, the proposed blade significantly reduced thermal accumulation during cutting (Fig. 19a), achieving a peak temperature (T_{peak}) of 43.3 °C, which was below the 47 °C cell damage threshold and lower than those of the two conventional blades (Fig. 19b,c). In contrast to the variation of trend Fz, the temperature rise exhibited a different trend. As shown in Fig. 20a, the trend Fz increased sharply during partial engagement and stabilized during full engagement. However, the temperature (Fig. 20b) continued to rise even after the force stabilized. This discrepancy indicates that thermal accumulation is governed not solely by instantaneous cutting force but also by chip evacuation efficiency and the thermal conductivity of the material. The prototype exhibited relatively low and stable temperature rise rates during both partial (11.75 °C/s) and full (11.25 °C/s) engagements, which highlight its superior heat dissipation capability under varying engagement conditions. In comparison, Con M1 and Con M2 showed significantly higher temperature rise rates, peaking at 24.00 °C/s for Con M1 during full engagement and 31.75 °C/

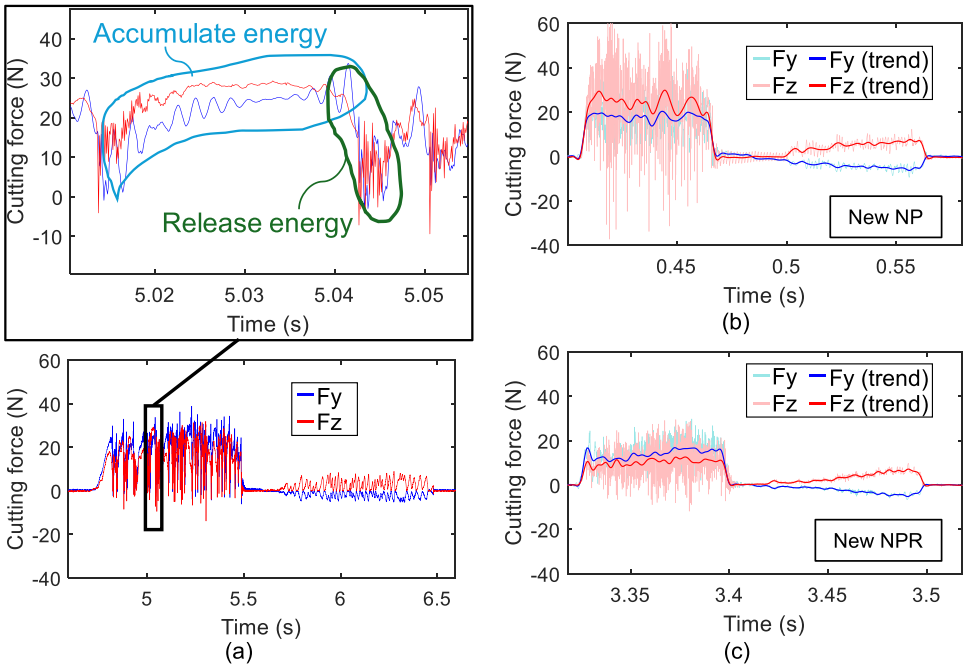

Fig. 16. Energy accumulation and release behavior during sawing with proposed blade configurations. (a) New P (oscillation frequency: 0.5 Hz, depth per cycle: 20 μm), showing a representative cycle of elastic energy accumulation followed by sudden release; (b) New NP and (c) New NPR (oscillation frequency: 5 Hz, depth per cycle: 20 μm). Trend forces (Fy and Fz) were extracted via low-pass filtering to highlight low-frequency variations. Corresponding sawing processes are presented in Supplementary Video 1.

s for Con M2 during partial engagement. Notably, although Con M2 produces lower sawing forces than Con M1, it yielded a higher peak temperature (Fig. 19c). This may be attributed to greater heat concentration near the tooth tip, caused by the presence of ploughing forces on both sides of the tooth throughout the sawing process. In comparison, Con M1 features a more inclined negative rake face, which provides a larger surface area for heat dissipation and allows for periodic cooling during cutting with the positive rake face. As a result, Con M2 exhibited a shorter temperature delay after sawing (Δs_3, Fig. 20b) and a shorter duration above the cell damage threshold (47 °C) of 3.9 s (Fig. 19c), which can be attributed to the rapid heat conduction through its high-thermal-conductivity blade material. In contrast, Con M1 showed a longer delay to the peak temperature (Δs_2, Fig. 20b) and a smaller post-sawing temperature increase (ΔT_2) than the prototype (ΔT_1), suggesting that heat accumulated in the retained chips (characterized by low thermal conductivity) was released more slowly. Consequently, the duration above 47 °C for Con M1 reached 4.4 s. On the other hand, the temperature difference between the center and side regions of the sawing area (ΔT_{peak}) was 1.9 °C for the prototype (Fig. 19a), indicating a more uniform thermal distribution compared to the conventional blades (approximately 5 °C, Fig. 19b,c).

Due to the spatial distance between the thermocouples and the saw blade, the recorded temperatures may underestimate the actual interfacial heat generated during cutting. To address this limitation, localized discoloration of bone powder residues compacted within Haversian canals (HC) and Volkmann's canals (VC) was analyzed as an indirect thermal indicator. In unheated bone, the collagen–mineral matrix remains intact exhibits high optical reflectivity and appears white under microscopy, as seen in the prototype result (Fig. 21a). However, when interfacial temperatures exceed approximately 60–70 °C, collagen denaturation and dehydration occur [38], disrupting the matrix structure and resulting in a yellowed appearance. Such discoloration was clearly observed in the groove wall surfaces machined by Con M1 and Con M2 (Fig. 21b,c), indicating localized thermal exposure exceeding the collagen denaturation threshold. To further investigate the nature of this discoloration, elemental analysis was performed on the yellowed regions and the adjacent unaffected groove wall in Con M1 (Fig. 21b), as well as on the white region and groove wall in Prototype (Fig. 21a). The elemental composition was similar across all regions, consisting mainly of O, Ca, and P, with only minor variations in content ratios. No exogenous elements were detected in the discolored zones. These results suggest that yellowing was not caused by elemental contamination but was instead a consequence of thermally induced collagen degradation, such as denaturation and dehydration.

Notably, the peak temperatures measured in this study were substantially lower than those reported by Micucci et al. [23], which exceeded 90 °C. The primary differences can be attributed to differences in cutting conditions. Their study employed a higher oscillation frequency (250 Hz) and a saw blade with a greater number of teeth (12 teeth, with a geometry resembling Con S2), both of which contributed to greater thermal accumulation. In contrast, the reduced peak temperatures observed in our experiments resulted from the combined effects of a reduced tooth count, increased gullet volume, lower oscillation frequency, and a larger depth per oscillation cycle—while maintaining a clinically relevant feed speed. These factors effectively suppressed thermal accumulation, but concurrently introduced challenges related to cutting-edge recession.

5.2.3. *Multi-tooth tip wear behavior*

Compared to the single-tooth tip wear behavior (Section 5.1.2), the tooth tip recession in multi-tooth sawing progressed more rapidly and severely for the conventional blades (Con M1 and Con M2). This accelerated wear is primarily attributed to altered cutting engagement caused by early tooth deformation, which increases the cutting depth of adjacent teeth and triggers progressive damage propagation (see Fig. 3), thereby increasing their cutting depth and inducing progressive damage propagation. In addition, excessive vibration between the blade and workpiece (Section 5.2.1) may have further contributed to wear acceleration. As a result, the conventional blades exhibited pronounced tip degradation even under a single 4 mm feed (Fig. 22b-e). In contrast, Prototype effectively suppressed tip recession (Fig. 22a,d,e): reducing the average recession distance variation from 67.3 μm to 7.6 μm, and the

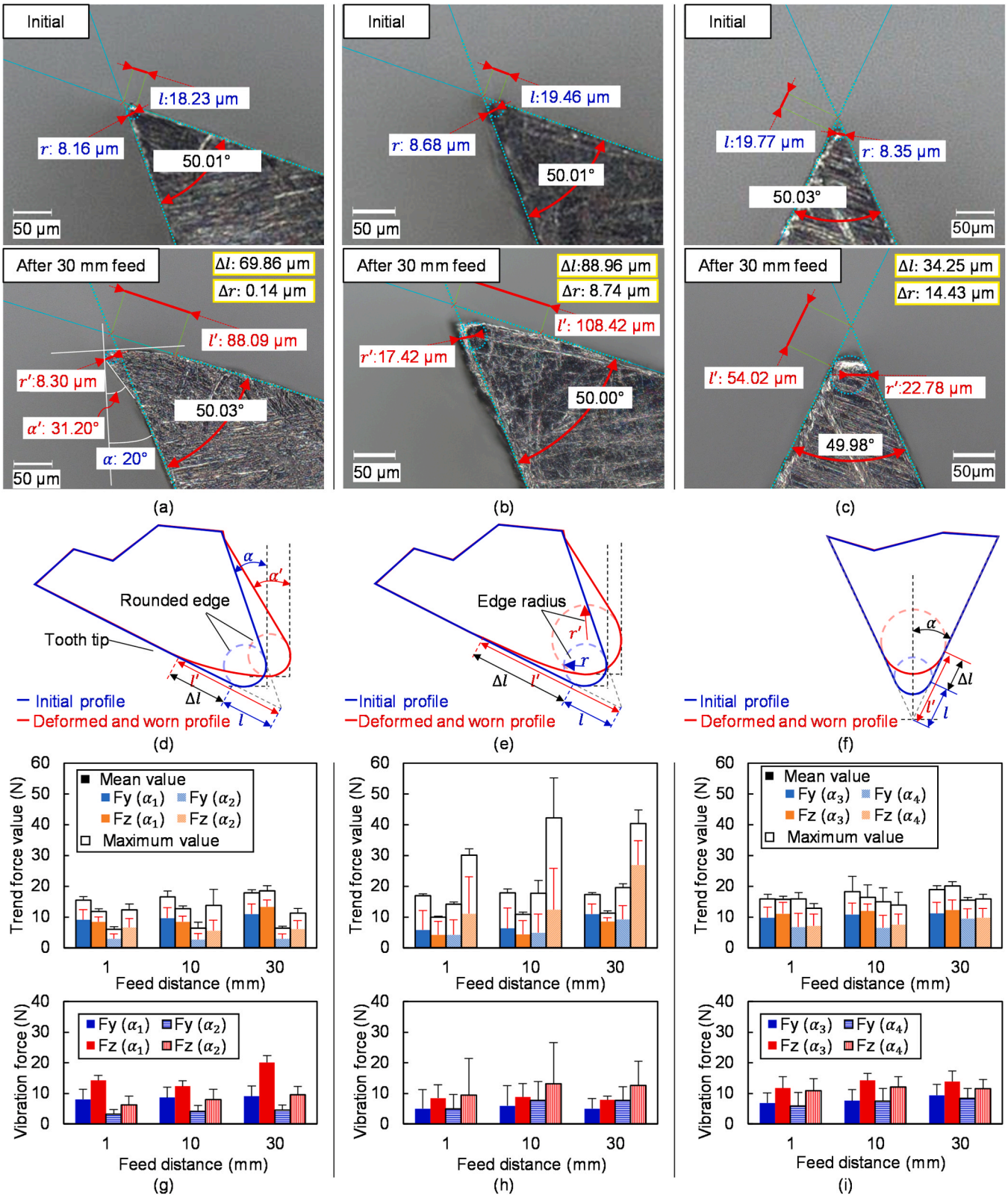

Fig. 17. Comparison of saw tooth wear characteristics for different blades: (a–c) optical images of tooth tips before and after cutting; (d–f) schematic diagrams of tip profile recession; (g–i) cutting force variations over feed cycles. Results correspond to (a, d, g) New NPR, (b, e, h) Con S1, and (c, f, i) Con S2. Cutting conditions: Total feed: 30 mm (1 mm per cutting cycle), oscillation frequency: 50 Hz. In (d–f), l denotes the projected distance from the ideal cutting edge (edge radius = 0) to the actual cutting edge along the flank face direction (initial edge radius ≈ 8 μm); l' represents the distance after cutting. Δl ($\Delta l = l' - l$) indicates edge recession due to deformation or wear. Error bars (shown on the positive side only) represent ±1 standard deviation.

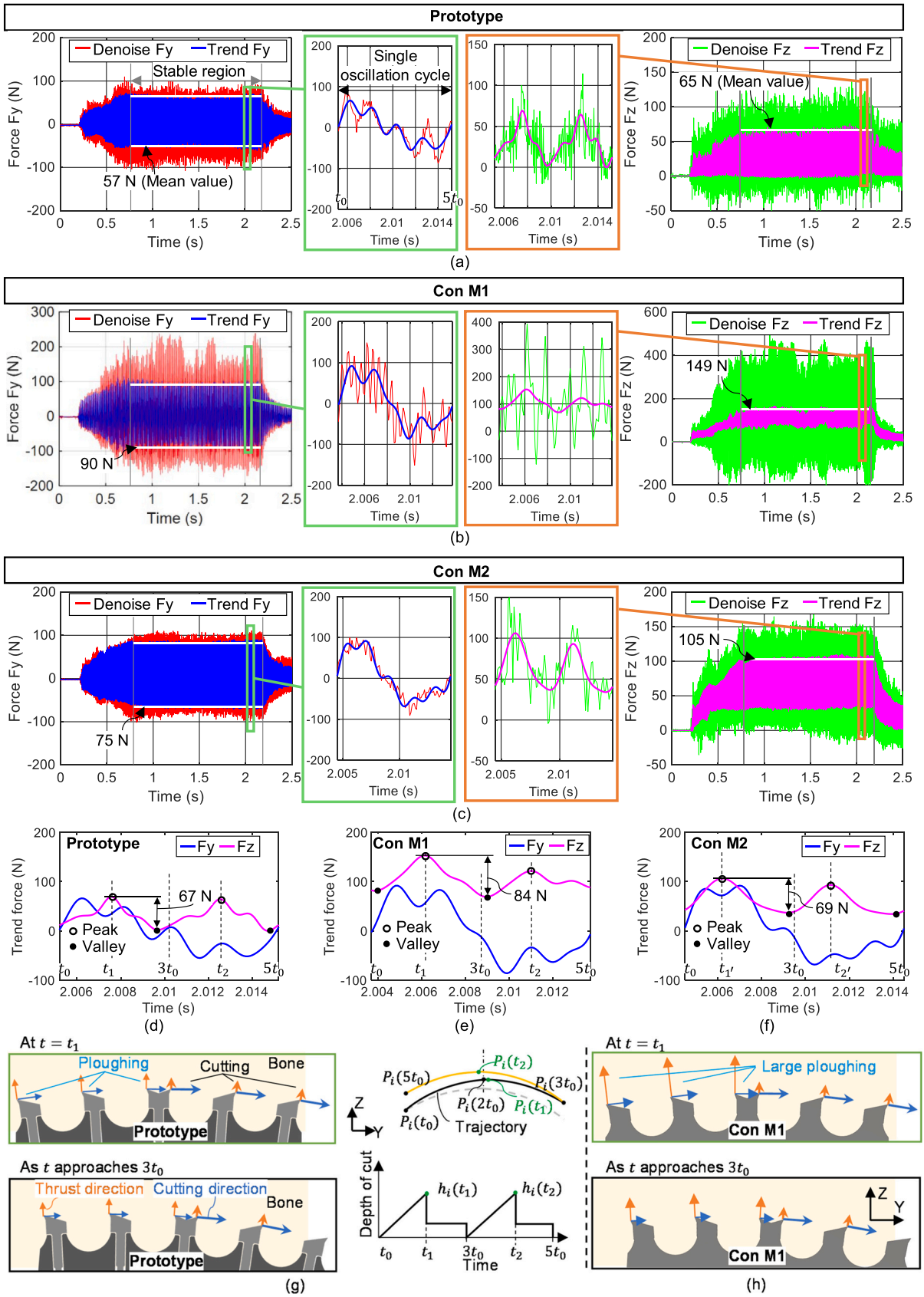

Fig. 18. Comparison of sawing forces during multi-tooth sawing experiments with different blades: (a–c) denoised Fy and Fz signals with corresponding trend curves; (d–f) trend force variations within a single oscillation cycle; (g, h) schematic diagrams of force components on tooth tips. Results correspond to (a, d, g) Prototype, (b, e, h) Con M1, and (c, f) Con M2. In (a–c), mean trend forces were calculated as the average peak values within the stable region. Peak and valley forces in each cycle were governed by the instantaneous cutting depth and reversal of cutting direction (see Fig. 3). Cutting conditions: oscillation frequency: 100 Hz; feed speed: 2 mm/s; cutting depth per oscillation cycle: 20 μm; total feed distance: 4 mm.

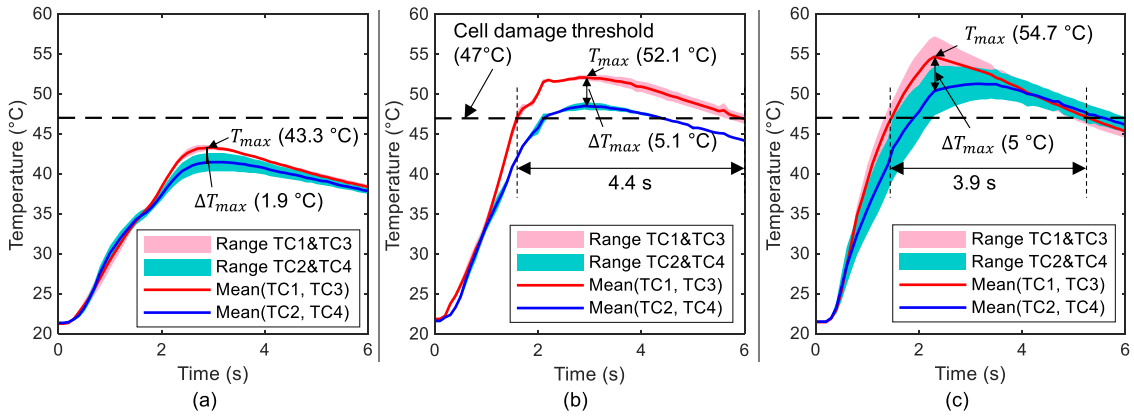

Fig. 19. Comparison of temperature rise during multi-tooth sawing experiments with different blades: (a) Prototype, (b) Con M1, and (c) Con M2. Temperature variations measured by thermocouples; shaded areas indicate temperature ranges between paired sensors (TC1 & TC3, TC2 & TC4), while solid lines represent their respective mean values. T_{peak}: peak temperature; ΔT_{peak}: maximum temperature difference between the middle and side regions of the sawing area.

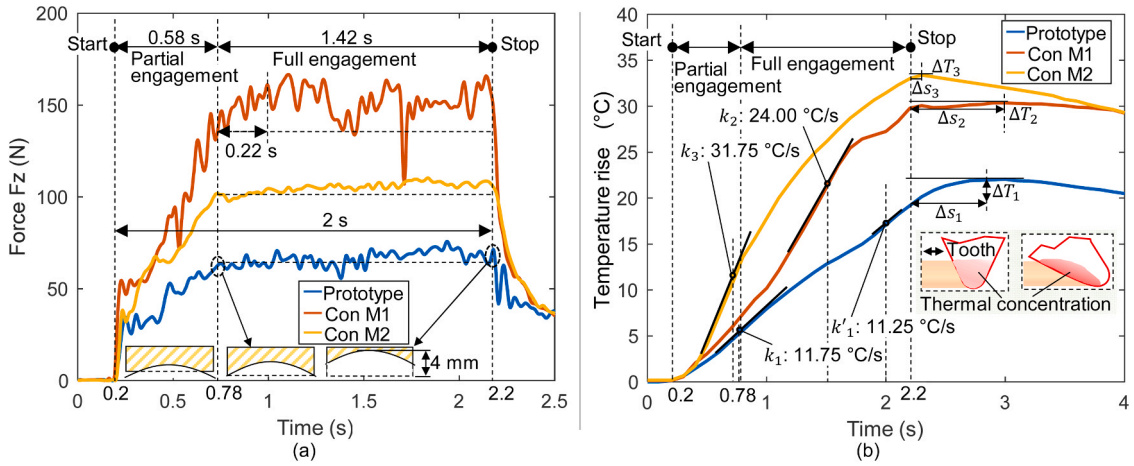

Fig. 20. Comparison of (a) trend force Fz (calculated by the upper envelope of the oscillatory force signals) and (b) temperature-rise profiles during multi-tooth sawing. k: maximum temperature rise rate; Δs, ΔT: time and temperature difference, respectively, between the end of sawing and the temperature peak.

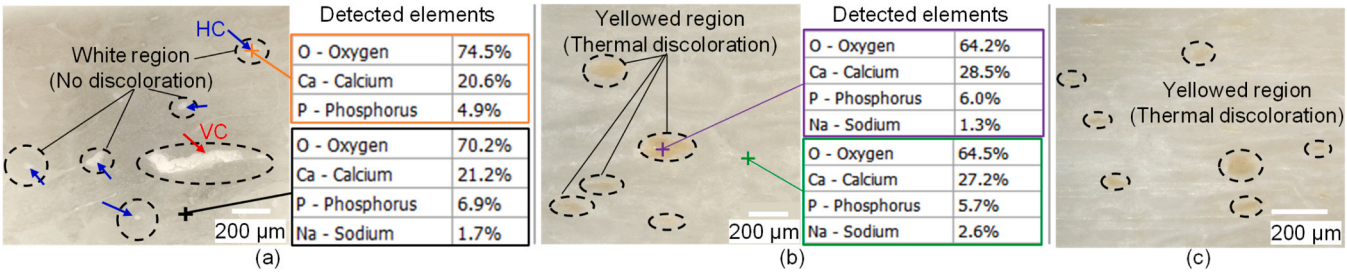

Fig. 21. Machined groove walls in the middle region of the sawing area using different blades: (a) Prototype, (b) Con M1, and (c) Con M2. Dashed circles indicate compacted bone powder within structural voids, exhibiting either no discoloration or a yellow tint from thermal effects. Elemental analysis was conducted at representative locations—(a) orange: white region; black: surrounding groove wall; (b) purple: yellowed region; green: surrounding groove wall—using laser-induced breakdown spectroscopy (LIBS). Despite visible color differences, the elemental composition remained largely consistent across these regions, suggesting that the discoloration was not due to elemental contamination but rather to thermally induced collagen denaturation and dehydration.

edge radius variation from 4.2 μm to 1.4 μm (Prototype vs. Con M1).

5.2.4. Chip morphology and evacuation performance

Consistent with the chip morphologies observed in the single-tooth sawing experiments (see Fig. 15), multi-tooth sawing with Prototype, Con M1 and Con M2 produced needle-like, spiral-like, and arc-like chips, respectively (Fig. 23a–c). Additionally, fine powder-like fragments were observed, possibly formed by fragmentation under high-frequency vibration and compressive stress. Among all those chip types, spiral-like chips exhibited the largest volume and the lowest breakability, making them particularly prone to compression and accumulation within the groove. In the case of Con M1, these chips even formed dense clusters that hindered the evacuation path (Fig. 23b).

Analysis of chip distribution and retained chip mass on the saw blades revealed that the proposed prototype exhibited superior fragmentation and evacuation performance, retaining only 5.2 mg of chips

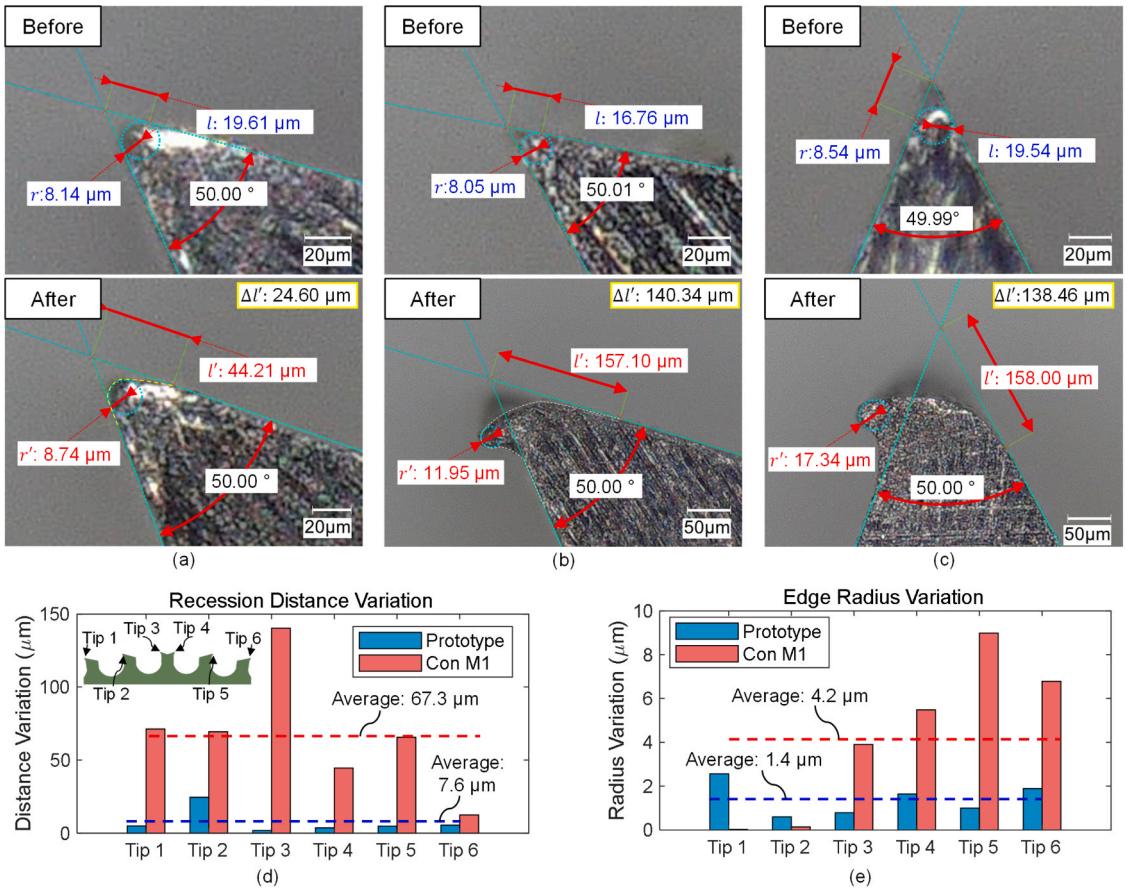

Fig. 22. Tooth tip recession before and after the multi-tooth sawing experiment with different blades: (a) Prototype, (b) Con M1, and (c) Con M2. (d) Recession distance variation, and (e) edge radius variation of each tooth tip, comparing Prototype and Con M1.

on the blade surface (Fig. 23d), compared to 20.0 mg for Con M1 and 15.1 mg for Con M2 (Fig. 23e,f). The substantial chip accumulation in conventional saw blades was probably caused by the consolidation of spiral- and arc-like chips under prolonged compression or mechanical entanglement. Although blade surface smoothness may slightly affect chip adhesion, the dominant factor is the increased resistance encountered by larger chips when passing through the narrow clearance between the blade and groove wall. Moreover, these retained chips possibly contributed to the elevated temperatures observed in Con M1 and Con M2 (Fig. 19b,c), by hindering heat dissipation and promoting thermal accumulation near the cutting zone.

5.2.5. *Crack morphology on machined surfaces*

To observe the actual crack morphologies, the groove regions were sectioned longitudinally using a thin circular saw, and the groove bottom were flattened by end milling. Representative results are shown in Fig. 24. In the prototype sample (Fig. 24a), only short and shallow cracks were observed on both the groove bottom and wall surfaces. In contrast, Con M1 produced longer and more cracks on both the bottom and wall (Fig. 24b). Regarding the groove bottom surface, Prototype produced a wavy profile (Fig. 24c), with a peak-to-valley height of approximately 11 μm and a wavelength of 100–200 μm, which corresponded well to the needle-like chips observed in Figs. 15h and 23a, indicating stable passive vibration-assisted cutting and periodic chip separation. On the other hand, Con M1 produced obvious ploughing marks (Fig. 24d), including pile-up regions (peak positive height: 22 μm) and sink-in regions (peak negative height: −26 μm), reflecting more severe tool–workpiece interaction and unstable cutting behavior.

Notably, cracks on the groove wall were consistently longer and more pronounced than those on the groove bottom in both blade types (Fig. 24), consistent with the crack propagation tendencies discussed in Section 2.2.

To further examine the depth of wall cracks, the groove walls were milled in 10 μm increments. After every 50 μm of total material removal, the newly exposed surface was examined via SEM. This stepwise procedure continued until no visible cracks were detected, enabling estimation of the crack propagation depth. Observations were made at the mid-region of the groove wall, deliberately avoiding zones near the thermocouple mounting holes, which could introduce artificial cracks due to local stress concentrations (Fig. 25).

Given that the typical osteon diameter ranges from 150 to 350 μm [39], the commonly used length threshold to distinguish microcracks (< 300 μm) from macrocracks (> 300 μm) [40] may correspond to whether a crack remains confined within a single osteon or propagates across multiple osteons. Macrocracks may form through the coalescence of microcracks and extend along osteon cement lines, representing a more critical form of structural compromise.

As shown in Fig. 25a–c, specimens processed by Prototype, Con M1, and Con M2 blades were progressively milled and examined. For comparison, Fig. 25d presents a reference surface milled from an adjacent region of the same specimen. Although narrow microcrack-like features were observed, they were sparse and can be attributable to the intrinsic bone microstructure, such as Volkmann's canals or cement lines, rather than sawing-induced damage.

Prototype (Fig. 25a) produced short and narrow cracks (typical length: 687 μm; width: 3.25 μm), which disappeared after 200 μm of milling, indicating shallow crack penetration. In contrast, Con M1 (Fig. 25b) induced longer and wider cracks (length: 1.95 mm; width: 6.73 μm), which disappeared after 400 μm of milling. Similarly, Con M2 (Fig. 25c) produced cracks with a length of approximately 1.2 mm and a

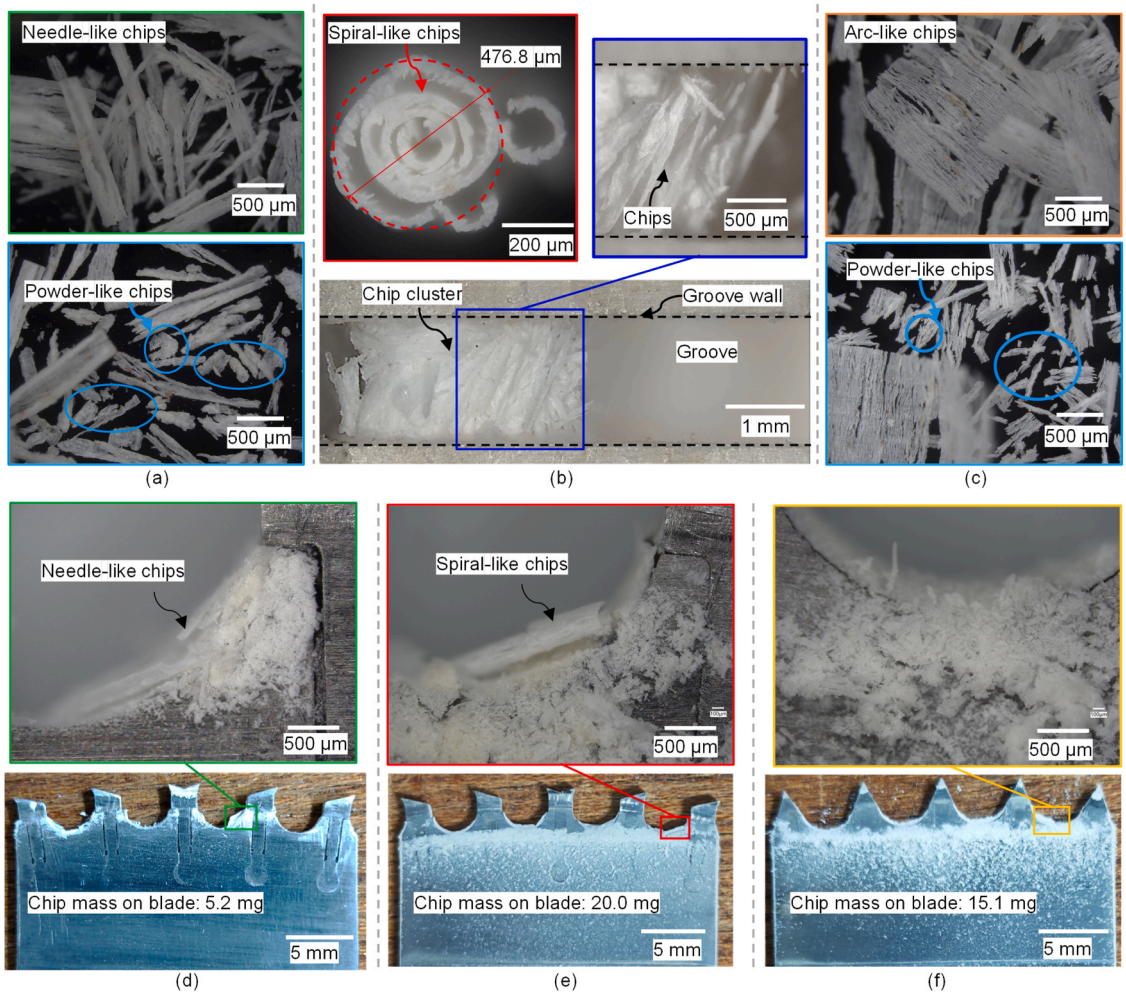

Fig. 23. Chip morphology and accumulation after multi-tooth sawing: (a–c) representative chip morphologies generated during cutting; (d–f) distribution of retained chips on the saw blades. Images correspond to (a, d) Prototype, (b, e) Con M1, and (c, f) Con M2. In (b), the spiral-like chips accumulated within the groove, forming dense chip clusters that hindered chip evacuation. Retained chip mass on blades: 5.2 mg (Prototype), 20.0 mg (Con M1), and 15.1 mg (Con M2).

width of 6.26 μm, extending to a depth of 350 μm. These results demonstrate that the proposed flexible-structured blade effectively suppresses both crack initiation and deep propagation, thereby reducing the risk of damage to regions critical for implant stability.

The proposed structural design and cutting strategy effectively mitigated the ploughing effects and enhanced chip evacuation, leading to lower cutting forces, reduced thermal loads, and improved resistance to tooth tip recession. These improvements highlight the potential for a more efficient and less invasive sawing process in clinical applications.

Nevertheless, limitations remain and warrant further discussion.

5.3. Limitations and future perspectives

Although silicone shows favorable durability, material wear or detachment may still occur under complex surgical conditions. While such issues may be less critical in single-use medical tools, the presence of a narrow slit increases the risk of local clogging and material degradation during extended use, which can compromise cutting performance. Therefore, further optimization of the slit geometry and filler material properties is essential to ensure reliable performance under demanding clinical conditions.

Another limitation is that forces acting along the blade thickness were not considered in this study. In clinical procedures, such forces are typically constrained by cutting guides or thicker blades (e.g., 2 mm in robotic systems). However, due to surgical variability and the irregular geometry of bone, deviations in cutting direction may occur, leading to unbalanced loading. This misalignment, similar to the skidding phenomenon in bone drilling [41], can induce tool deformation, increased cutting forces and heat generation. For flexible-structured blades, which are susceptible to deformation, the influence of such out-of-plane forces and their structural response under surgical conditions require further investigation.

Future improvement of the tooth tip geometry may involve the use of multiple micro-edge features [42] to generate smaller, powder-like chips, thereby facilitating chip evacuation. Although this approach may slightly increase cutting forces, it presents a promising direction for improving chip control and overall cutting performance.

While the current tooth structure was fabricated via wire-cut EDM, powder metallurgy offers a potential alternative for improved manufacturing efficiency. The use of functionally graded materials (FGMs) may also enable a tough, high-strength shank combined with a hard, wear-resistant tooth tip [43], further mitigating tip recession. Conventional blades have primarily focused on wear resistance, but their inability to reduce ploughing force limits their effectiveness in reducing cutting force and heat generation. In contrast, the proposed design reduces ploughing force via structural deformation, enabling improvement in both durability and cutting efficiency. These developments may also inspire new strategies for manufacturing and recycling orthopedic saw blades, particularly for single-use applications.

Beyond orthopedics, the proposed structure may be adapted to

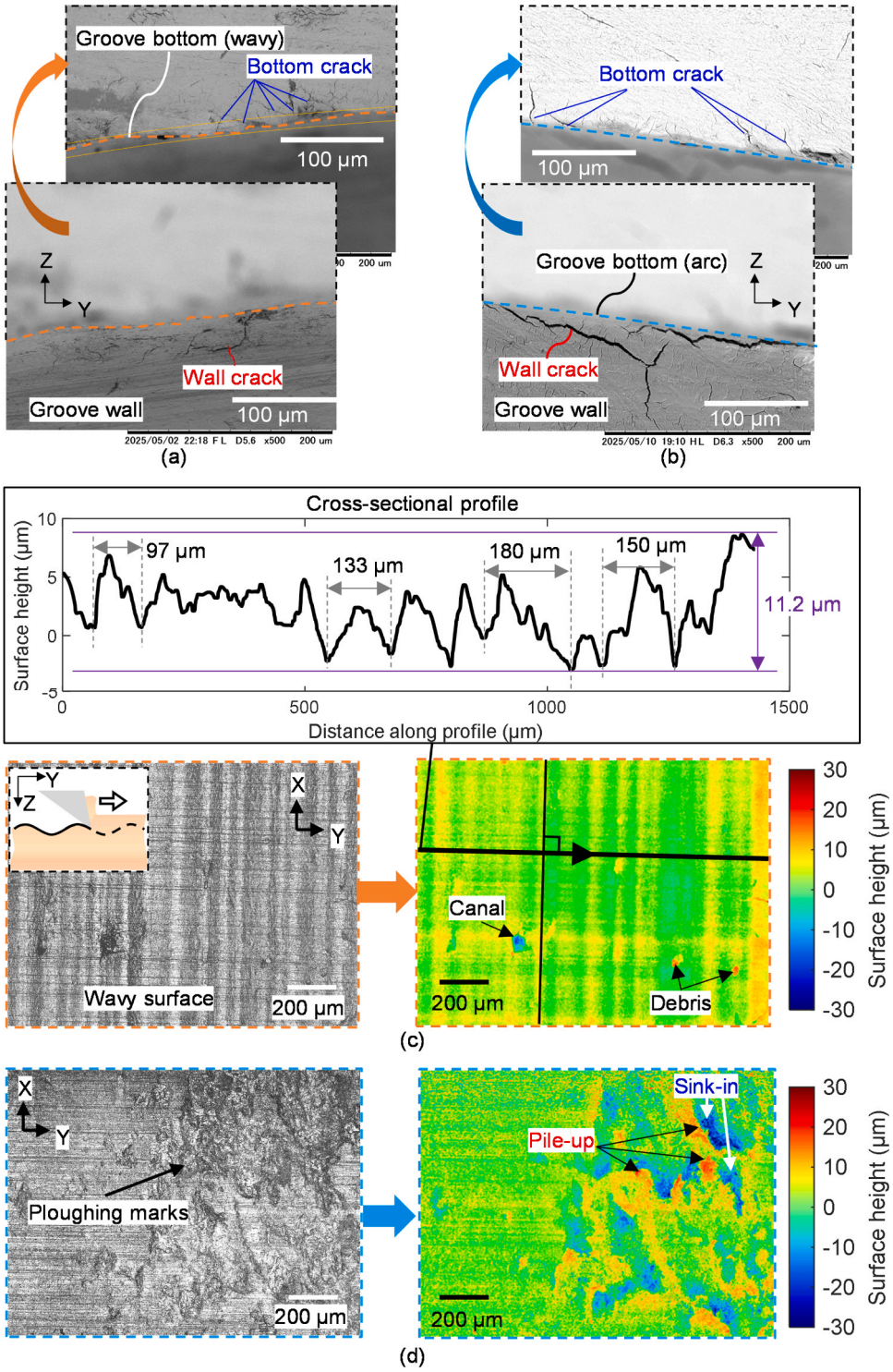

Fig. 24. Crack morphology on the machined groove wall surfaces and cross-sectional view of the groove bottom (a, b), and corresponding 3D surface topography of the groove bottom (c, d) after multi-tooth sawing, for Prototype (a, c) and Con M1 (b, d).

reciprocating saws used in woodworking and composite material processing. Its ability to promote chip formation and evacuation also makes it suitable for rotary or band saws in dense or layered materials. Furthermore, this flexible structural concept may be appearing oscillatory cutting tools, such as oscillating milling systems designed to reduce soft tissue entanglement during surgery [2]. Therefore, the proposed design offers broad potential as a tool optimization strategy for oscillatory and reciprocating cutting applications.

6. Conclusions

In this study, a novel saw blade incorporating an embedded flexible hinge structure was proposed to address both ploughing effects and chip accumulation in oscillating bone sawing. Mechanism analysis and single-tooth sawing experiments revealed that, under negative rake engagement, the passive rotation of the tooth tip adaptively reduced the effective cutting depth, leading to ploughing force reductions of at least 61 % in the oscillation direction and 73 % in the feed direction. Under

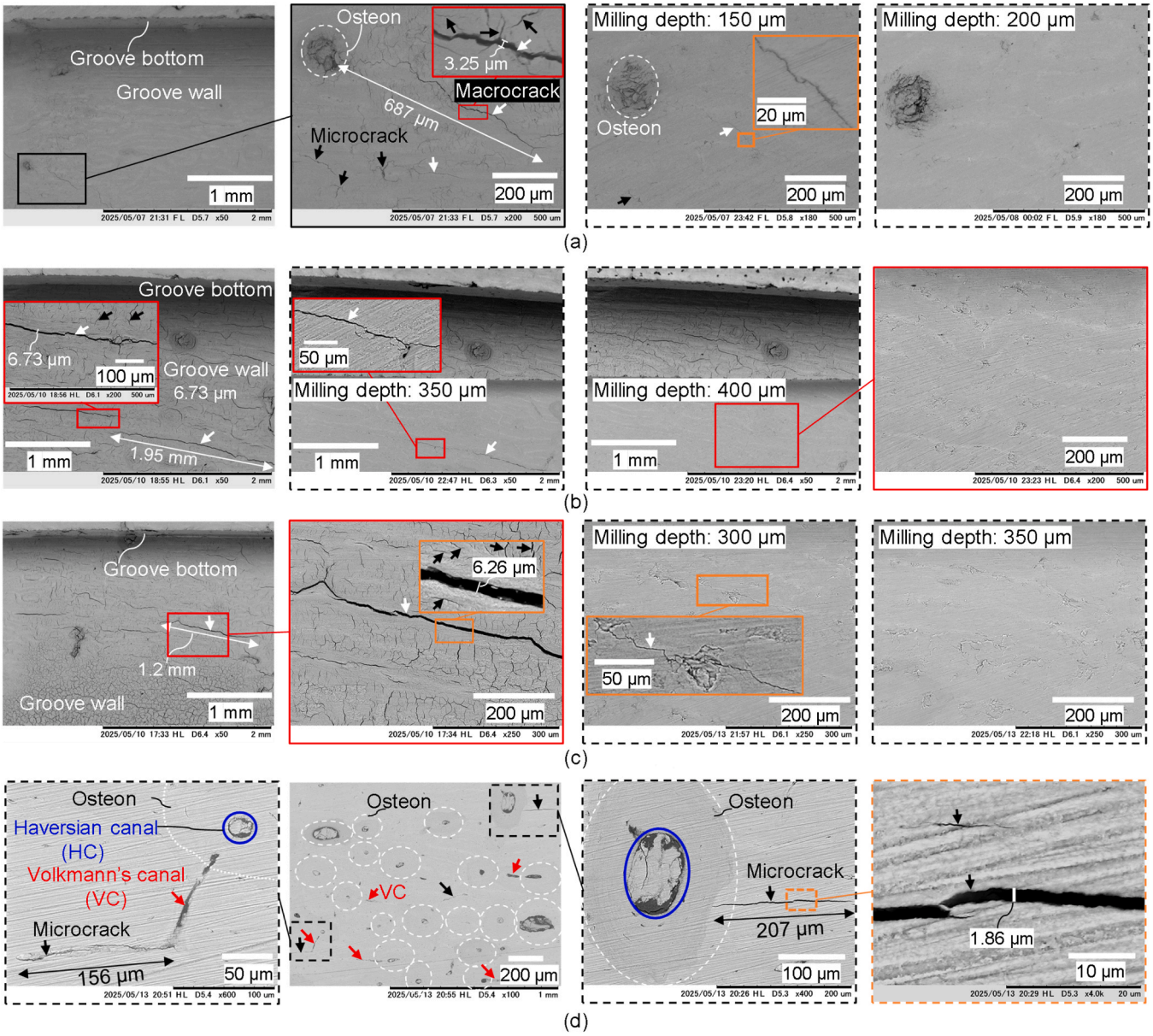

Fig. 25. SEM images of groove wall surfaces after progressive milling to evaluate crack depth: (a) Prototype, (b) Con M1, and (c) Con M2. Milling was performed in 10 μm increments, and SEM observations were conducted at every 50 μm interval in the mid-region of the groove wall (avoiding areas adjacent to thermocouple holes). Typical crack dimensions: (a) length: 687 μm, width: 3.25 μm, depth < 200 μm; (b) length: 1.95 mm, width: 6.73 μm, depth < 400 μm; (c) length: 1.2 mm, width: 6.26 μm, depth < 350 μm. (d) Reference surface prepared from an adjacent area of the same specimen, showing sparse, narrow microcrack-like features attributed to bone microstructure (e.g., Volkmann's canals) or minor artifacts, clearly distinct from the sawing-induced macrocracks observed in (a–c).

positive rake engagement, elastic deformation of the flexible tooth shank enabled energy accumulation and release, promoting crack propagation along the shear plane and transforming continuous, spiral-like chips (diameter: 489 μm) into fragmented, needle-like chips (width: 150 μm), thereby enhancing chip evacuation through the limited clearance. A multi-tooth prototype was fabricated and experimentally validated under practical sawing conditions. Compared to conventional blades, the proposed design reduced cutting forces by 56.4 % and 36.7 % in the feed and oscillation directions, respectively, while lowering the peak temperature to 43.3 °C—below the bone cell damage threshold of 47 °C. It also improved chip evacuation (74 % reduction in retained chip mass on blade), wear resistance (89 % reduction in tooth tip recession), and crack suppression (50 % reduction in groove wall crack depth).

These results demonstrate that incorporating flexible structures into cutting tools can modulate energy accumulation and release during chip formation, leading to altered chip morphology and continuity. This passive, structure-induced effect provides a compact alternative to externally actuated vibration-assisted cutting methods, which typically require additional hardware and control systems. The proposed concept is particularly suited for oscillatory cutting tools in orthopedic applications (e.g., milling, drilling), and holds promise for broader use in the machining of hard, brittle, or layered materials where chip segmentation is challenging.

CRediT authorship contribution statement

Han Wang: Writing – original draft, Validation, Methodology, Data curation, Conceptualization. **Urara Satake:** Writing – review & editing, Supervision, Investigation. **Toshiyuki Enomoto:** Writing – review & editing, Supervision, Resources, Investigation, Funding acquisition.

Declaration of Competing Interest

The authors declare the following financial interests/personal relationships which may be considered as potential competing interests: Han Wang, Urara Satake, Toshiyuki Enomoto has patent #PCT/JP2024/042614 pending to The University of Osaka. If there are other authors, they declare that they have no known competing financial interests or personal relationships that could have appeared to influence the work reported in this paper.

Acknowledgments

This study was supported by a Grant-in-Aid for Scientific Research (No. 24K00777, 2024) from the Ministry of Education, Culture, Sports, Science and Technology (MEXT), Japan; and by the Osawa Scientific Studies Grants Foundation, Japan.

Appendix A. Supporting information

Supplementary data associated with this article can be found in the online version at doi:10.1016/j.jmatprotec.2025.119000.

References

[1] James, T.P., Pearlman, J.J., Saigal, A., 2013. Predictive force model for haptic feedback in bone sawing. Med Eng. Phys. 35, 1638–1644. https://doi.org/10.1016/j.medengphy.2013.05.012.
[2] Bono, P.L., Lark, J.D., Freimark, C.A., Ruhala, A.J., 2022. Rotary Oscil. Bone Cartil. Disk Remov. Tool. Assem.(accessed April 20, 2025).⟨https://patents.google.com/patent/US20250040941A1/en?oq=US20250040941A1⟩(accessed April 20, 2025)..
[3] Wang, H., Satake, U., Enomoto, T., 2024. Reduction of sawing forces in bone cutting: innovative oscillating saw mechanism based on trajectory analysis. J. Mater. Process Technol. 332, 118563. https://doi.org/10.1016/J.JMATPROTEC.2024.118563.
[4] Plaskos, C., Hodgson, A.J., Inkpen, K., McGraw, R.W., 2002. Bone cutting errors in total knee arthroplasty. J. Arthroplast. 17, 698–705. https://doi.org/10.1054/arth.2002.33564.
[5] Wang, H., Satake, U., Enomoto, T., 2022. Surgical oscillating saw blade to suppress forces in bone cutting. CIRP Ann. 71, 73–76. https://doi.org/10.1016/j.cirp.2022.04.066.
[6] Robles-Linares, J.A., Axinte, D., Liao, Z., Gameros, A., 2021. Machining-induced thermal damage in cortical bone: necrosis and micro-mechanical integrity. Mater. Des. 197, 109215. https://doi.org/10.1016/J.MATDES.2020.109215.
[7] James, T.P., Chang, G., Micucci, S., Sagar, A., Smith, E.L., Cassidy, C., 2014. Effect of applied force and blade speed on histopathology of bone during resection by sagittal saw. Med Eng. Phys. 36, 364–370. https://doi.org/10.1016/J.MEDENGPHY.2013.12.002.
[8] Kluess, D., Bergschmidt, P., Mueller, I., Mittelmeier, W., Bader, R., 2012. Influence of the distal femoral resection angle on the principal stresses in ceramic total knee components. Knee 19, 846–850. https://doi.org/10.1016/J.KNEE.2012.03.014.
[9] Zhang, Y., Robles-Linares, J.A., Chen, L., Liao, Z., Shih, A.J., Wang, C., 2022. Advances in machining of hard tissues – from material removal mechanisms to tooling solutions. Int J. Mach. Tools Manuf. 172, 103838. https://doi.org/10.1016/j.ijmachtools.2021.103838.
[10] Launey, M.E., Buehler, M.J., Ritchie, R.O., 2010. On the mechanistic origins of toughness in bone. Annu Rev. Mater. Res 40, 25–53. https://doi.org/10.1146/annurev-matsci-070909-104427.
[11] Liao, Z., Axinte, D.A., 2016. On chip formation mechanism in orthogonal cutting of bone. Int J. Mach. Tools Manuf. 102, 41–55. https://doi.org/10.1016/J.IJMACHTOOLS.2015.12.004.
[12] H. Peterlik, P. Roschger, K. Klaushofer, P. Fratzl, From brittle to ductile fracture of bone, (2005). https://doi.org/10.1038/nmat1545.
[13] Schwiedrzik, J., Raghavan, R., Bürki, A., Lenader, V., Wolfram, U., Michler, J., Zysset, P., 2014. In situ micropillar compression reveals superior strength and ductility but an absence of damage in lamellar bone, 13 Nat. Mater. 2014 13 (7), 740–747. https://doi.org/10.1038/nmat3959.
[14] Wang, H., Satake, U., Enomoto, T., 2023. Serrated chip formation mechanism in orthogonal cutting of cortical bone at small depths of cut. J. Mater. Process Technol. 319. https://doi.org/10.1016/j.jmatprotec.2023.118097.
[15] Sugita, N., Osa, T., Aoki, R., Mitsuishi, M., 2009. A new cutting method for bone based on its crack propagation characteristics. CIRP Ann. 58, 113–118. https://doi.org/10.1016/J.CIRP.2009.03.057.
[16] Sugita, N., Mitsuishi, M., 2009. Specifications for machining the bovine cortical bone in relation to its microstructure. J. Biomech. 42, 2826–2829. https://doi.org/10.1016/J.JBIOMECH.2009.08.017.
[17] Alam, K., Mitrofanov, A.V., Silberschmidt, V.V., 2011. Experimental investigations of forces and torque in conventional and ultrasonically-assisted drilling of cortical bone. Med Eng. Phys. 33, 234–239. https://doi.org/10.1016/J.MEDENGPHY.2010.10.003.
[18] Sugita, N., Ishii, K., Sui, J., Terashima, M., 2014. Multi-grooved cutting tool to reduce cutting force and temperature during bone machining. CIRP Ann. 63, 101–104. https://doi.org/10.1016/J.CIRP.2014.03.069.
[19] Liao, Z., Axinte, D.A., Gao, D., 2017. A novel cutting tool design to avoid surface damage in bone machining. Int J. Mach. Tools Manuf. 116, 52–59. https://doi.org/10.1016/J.IJMACHTOOLS.2017.01.003.
[20] Bai, W., Shu, L., Sun, R., Xu, J., Silberschmidt, V.V., Sugita, N., 2020. Improvements of material removal in cortical bone via impact cutting method. J. Mech. Behav. Biomed. Mater. 108, 103791. https://doi.org/10.1016/J.JMBBM.2020.103791.
[21] Bai, W., Zhai, Y., Zhao, J., Han, G., Ye, L., Zhu, X., Shu, L., Wang, D., 2023. Experimental investigation of material removal in elliptical vibration cutting of cortical bone. Chin. J. Mech. Eng. (Engl. Ed.) 36, 1–10. https://doi.org/10.1186/S10033-023-00879-5/FIGURES/10.
[22] Wang, H., Satake, U., Enomoto, T., 2024. Modeling of oscillating bone sawing forces with instantaneous cutting speed and depth of cut. J. Mater. Process Technol. 324, 118225. https://doi.org/10.1016/J.JMATPROTEC.2023.118225.
[23] Micucci, S., Chang, G., Smith, E., Cassidy, C., Sagar, A., James, T.P., 2014. Effect of oscillation speed and thrust force on cortical bone temperature during sagittal sawing. ASME Int. Mech. Eng. Congr. Expo. Proc. (IMECE) 3 A. https://doi.org/10.1115/IMECE2013-62556.
[24] Liao, Z., Axinte, D., Gao, D., 2019. On modelling of cutting force and temperature in bone milling. J. Mater. Process Technol. 266, 627–638. https://doi.org/10.1016/J.JMATPROTEC.2018.11.039.
[25] James, T.P., Pearlman, J.J., Saigal, A., 2012. Rounded cutting edge model for the prediction of bone sawing forces. J. Biomech. Eng. 134. https://doi.org/10.1115/1.4006972.
[26] Enomoto, T., Shigeta, H., Sugihara, T., Satake, U., 2014. A new surgical grinding wheel for suppressing grinding heat generation in bone resection. CIRP Ann. 63, 305–308. https://doi.org/10.1016/J.CIRP.2014.03.026.
[27] James, T.P., Kelly, M.P., Lannin, T.B., Pearlman, J.J., Saigal, A., 2013. Sagittal bone saw with orbital blade motion for improved cutting efficiency. J. Med. Devices Trans. ASME 7. https://doi.org/10.1115/1.4023500/376527.
[28] Shu, L., Sugita, N., Oshima, M., Mitsuishi, M., 2018. Design and experimental force analysis of a novel elliptical vibration assisted orthopedic oscillating saw. Med Eng. Phys. 54, 22–31. https://doi.org/10.1016/j.medengphy.2018.02.005.
[29] Shu, L., Sugita, N., 2020. Analysis of fracture, force, and temperature in orthogonal elliptical vibration-assisted bone cutting. J. Mech. Behav. Biomed. Mater. 103, 103599. https://doi.org/10.1016/J.JMBBM.2019.103599.
[30] Zawadzki, P., Talar, R., Patalas, A., Legutko, S., 2022. Influence of machining parameters on cutting and Chip-Formation process during cortical bone orthogonal machining. Materials 15, 6414. https://doi.org/10.3390/ma15186414.
[31] Bai, W., Shu, L., Sun, R., Xu, J., Silberschmidt, V.V., Sugita, N., 2020. Mechanism of material removal in orthogonal cutting of cortical bone. J. Mech. Behav. Biomed. Mater. 104, 103618. https://doi.org/10.1016/j.jmbbm.2020.103618.
[32] Bergman, T.L., 2011. Fundamentals of heat and mass transfer. John Wiley & Sons.
[33] Feldmann, A., Ganser, P., Nolte, L., Zysset, P., 2017. Orthogonal cutting of cortical bone: temperature elevation and fracture toughness. Int J. Mach. Tools Manuf. 118119 1–11. https://doi.org/10.1016/J.IJMACHTOOLS.2017.03.009.
[34] Goldfarb, M., Speich, J.E., 1999. A well-behaved revolute flexure joint for compliant mechanism design. J. Mech. Des. 121, 424–429. https://doi.org/10.1115/1.2829478.
[35] Bai, X., Hou, S., Li, K., Qu, Y., Zhu, W., 2020. Analysis of machining process and thermal conditions during vibration-assisted cortical bone drilling based on generated bone chip morphologies. Med Eng. Phys. 83, 73–81. https://doi.org/10.1016/j.medengphy.2020.07.016.
[36] Wang, J., Satake, U., Enomoto, T., 2025. Mechanisms of cutting soft tissues using snare-type tools. Med Eng. Phys. 138, 104314. https://doi.org/10.1016/J.MEDENGPHY.2025.104314.
[37] Chen, Y.C., Tsai, Y.J., Hsiao, H.Y., Chiu, Y.W., Hong, Y.Y., Tu, Y.K., Hsiao, C.K., 2024. Assessment of thermal osteonecrosis during bone drilling using a three-dimensional finite element model. Bioengineering 2024 11 (11), 592. https://doi.org/10.3390/BIOENGINEERING11060592.

[38] Lambri, M.L., Bozzano, P.B., Giordano, E.D.V., Bonifacich, F.G., Gargicevich, D., Zelada, G.I., Lambri, O.A., 2018. Denaturation processes of collagen from cow bones as a function of temperature. Mat. éria (Rio De. Jan.) 23, e12089. https://doi.org/10.1590/S1517-707620180002.0424.

[39] van Oers, R.F.M., Ruimerman, R., van Rietbergen, B., Hilbers, P.A.J., Huiskes, R., 2008. Relating osteon diameter to strain. Bone 43, 476–482. https://doi.org/10.1016/J.BONE.2008.05.015.

[40] O'Brien, F.J., Taylor, D., Lee, T.C., 2005. The effect of bone microstructure on the initiation and growth of microcracks. J. Orthop. Res. 23, 475–480. https://doi.org/10.1016/J.ORTHRES.2004.08.005.

[41] Shu, L., Li, S., Terashima, M., Bai, W., Hanami, T., Hasegawa, R., Sugita, N., 2020. A novel self-centring drill bit design for low-trauma bone drilling. Int J. Mach. Tools Manuf. 154, 103568. https://doi.org/10.1016/J.IJMACHTOOLS.2020.103568.

[42] Gao, P., Wang, J., Sun, T., Wang, M., Zan, T., Zhao, X., 2024. Cutting performance of multi-tooth milling cutter for cortical bone longitudinal torsional ultrasonic vibration assisted cutting. Compos. Adv. Mater. 33. https://doi.org/10.1177/26349833241303521.

[43] Yadav, S., Liu, S., Singh, R.K., Sharma, A.K., Rawat, P., 2024. A state-of-art review on functionally graded materials (FGMs) manufactured by 3D printing techniques: advantages, existing challenges, and future scope. J. Manuf. Process 131, 2051–2072. https://doi.org/10.1016/J.JMAPRO.2024.10.026.